Slow Slip Predictions Based on Granit and Gabbro Friction Data Compared to GPS Measurements in Northern Cascadia

JOURNAL OF GEOPHYSICAL RESEARCH, VOL. 114, B09407, doi:10.1029/2008JB006142, 2009

Slow slip predictions based on granite and gabbro friction data compared to GPS measurements in northern Cascadia

Yajing Liu[1] and James R. Rice[2]

Received 7 October 2008; revised 17 April 2009; accepted 12 June 2009; published 29 September 2009.

[1] For episodic slow slip transients in subduction zones, a large uncertainty in comparing surface deformations predicted by forward modeling based on rate and state friction to GPS measurements lies in our limited knowledge of the frictional properties and fluid pore pressure along shallow subduction faults. In this study, we apply the laboratory rate and state friction data of granite and gabbro gouges under hydrothermal conditions to a Cascadia-like 2-D model to produce spontaneous aseismic transients, and we compare the resulting intertransient and transient surface deformations to GPS observations along the northern Cascadia margin. An inferred region along dip of elevated fluid pressure is constrained by seismological observations where available and by thermal and petrological models for the Cascadia and SW Japan subduction zones. For the assumed friction parameters a and $a - b$ profiles, we search the model parameter space, by varying the level of effective normal stress $\bar{\sigma}$, characteristic slip distance L in the source areas of transients, and the fault width under $\bar{\sigma}$, to identify simulation cases that produce transients of total aseismic slip and recurrence interval similar to the observed 20–30 mm and 1–2 years, respectively, in northern Cascadia. Using a simple planar fault geometry and extrapolating the 2-D fault slip to a 3-D distribution, we find that the friction data for gabbro gouge, a better representation of the seafloor, fit GPS observations of transient deformation in northern Cascadia much better than do the granite data, which, for lack of a suitable alternative, have been the basis for most previous modeling.

Citation: Liu, Y., and J. R. Rice (2009), Slow slip predictions based on granite and gabbro friction data compared to GPS measurements in northern Cascadia, *J. Geophys. Res.*, *114*, B09407, doi:10.1029/2008JB006142.

1. Introduction

[2] Episodic slow slip events (SSE) have been observed in shallow subduction zones [*Hirose et al.*, 1999; *Dragert et al.*, 2001; *Lowry et al.*, 2001; *Schwartz and Rokosky*, 2007], transform plate boundaries [*Linde et al.*, 1996; *Murray and Segall*, 2005], and megalandslide faults associated with volcanoes [*Segall et al.*, 2006; *Brooks et al.*, 2006]. In subduction zones, episodic surface deformation reversals that last a few days to weeks are estimated to be results of a few millimeters to centimeters of accelerated thrust slip on the subduction plate interface near or downdip from the seismogenic zone, suggesting an averaged slip rate 1–2 orders of magnitude higher than the plate convergence rate V_{pl}. The actual slip rate may be greater, because the duration when the signal is observed at a particular GPS station is most likely larger than the duration of slip directly beneath the station. Slow slip migrates along the strike direction at average speeds of 5–15 km/d in the Cascadia, southwest Japan and Guerrero, Mexico, subduction zones. Recurrence intervals of a few months to several years are observed at plate boundaries with long-term continuous geodetic monitoring.

[3] In Cascadia and SW Japan, slow slip events are accompanied by low-frequency deep nonvolcanic tremors that are most energetic between 1 and 10 Hz [*Obara*, 2002; *Rogers and Dragert*, 2003; *Kao et al.*, 2006]. Tremors correlate very well in time and epicentral depths with slow slip events, but the accurate hypocenters are difficult to locate by conventional techniques due to the absence of clear impulsive onset phases. In Japan, beneath Shikoku Island, low-frequency earthquakes (LFE) with emergent S arrivals have been identified among the tremor waveforms, allowing more precise relocation of LFE sources on or near the plate interface [*Shelly et al.*, 2006, 2007], consistent with the depths where slow slip events take place. Focal mechanism analysis of LFEs in Japan also indicates shear slip on a shallow thrust fault in the direction of plate subduction [*Ide et al.*, 2007], suggesting that tremor and slow slip are manifestations of the same physical process on the plate interface. However, different tremor relocation studies in Cascadia showed different depth distributions, possibly due to the absence of LFEs in tremor signals.

[1]Department of Geosciences, Princeton University, Princeton, New Jersey, USA.
[2]Department of Earth and Planetary Sciences and School of Engineering and Applied Sciences, Harvard University, Cambridge, Massachusetts, USA.

0148-0227/09/2008JB006142$09.00

Using a source scanning algorithm [*Kao et al.*, 2005], *Kao et al.* [2006] found that tremor sources are broadly distributed between depths 10 and 50 km, mostly above the subduction plate in northern Cascadia. On the contrary, a recent relocation study using S minus P wave times as constraints showed most of them locate near the subduction interface [*La Rocca et al.*, 2009], similar to the tremor distributions in SW Japan.

[4] Several physical mechanisms have been proposed for generating spontaneous slow slip events in the framework of rate- and state-dependent friction laws. In modeling the earthquake preparation process in subduction zones, *Kato* [2003] and *Shibazaki and Iio* [2003] introduced a small aseismic cutoff velocity V_c to the evolution effect in the friction law at depths below the seismogenic zone, such that friction oscillates between velocity weakening (potentially unstable) when slip rate V is lower than V_c and velocity strengthening (stable) when V is greater than V_c. The regulation effect of V_c allows slow slip events to appear with similar velocities. However, such assumption about the constitutive response was based on friction experiments on dolomite [*Weeks and Tullis*, 1985] and halite [*Shimamoto*, 1986] at room temperatures, thus it is not clear how the mechanism would be at higher temperatures appropriate for SSE modeling. In addition, while the cutoff velocity for halite experiments is around 10^{-6} to 10^{-5} m/s, an opposite transition from velocity strengthening to weakening was observed at low velocities around 10^{-8} m/s, comparable to plate convergence rates and presumably more realistic for modeling displacement on a subduction fault loaded by $V_{pl} \sim 10^{-9}$ m/s. *Liu and Rice* [2005a, 2007] applied temperature, hence depth-variable wet granite rate and state friction parameters [*Blanpied et al.*, 1998] in their 2-D and 3-D subduction earthquake models with the "ageing" version of evolution law, and produced episodic slow slip events when the velocity-weakening fault length W under highly elevated pore pressure is too large for steady sliding but insufficient for dynamic instability [*Liu and Rice*, 2007]; the fault response is dominated by the ratio between W and the critical nucleation size h^*. With a similar model setup, *Rubin* [2008] found that spontaneous SSEs also arise with the "slip" evolution law but for a much smaller range of W/h^*. Different versions of evolution laws and the detailed definition of h^* will be described in section 2. Another mechanism for producing SSEs on a velocity-weakening fault over a much broader W/h^* range is to involve fault gouge dilatancy, a stabilizing interaction between pore fluids and slip that is shown to be most significant at high pore pressure [*Segall and Rice*, 1995; *Segall and Rubin*, 2007]. The possible effects of dilatancy on slow slip events and megathrust earthquakes are currently under investigation [*Liu et al.*, 2008] and are briefly discussed in section 5.

[5] For the above proposed mechanisms, numerical simulations predict spontaneous aseismic deformation transients with aspects that agree reasonably well with SSE observations. *Liu and Rice* [2007] found that for fixed friction parameter distributions with depth and constant W/h^*, the SSE recurrence interval increases with the level of effective normal stress $\bar{\sigma}$, the difference between lithostatic normal stress σ and pore fluid pressure p. They showed that in a simplified Cascadia-like model with temperature-dependent wet granite friction data, a 1–2 year period is achieved at $\bar{\sigma} \sim 2$–3 MPa for simple periodic aseismic slip events. The total amount of slip on the subduction interface is about 1–2 cm per episode. However, the horizontal surface deformation based on the modeled fault slip is significantly smaller than the observations at most GPS stations in northern Cascadia. Further, the modeled aseismic moment is contributed over a zone extending mostly updip and only slightly downdip from the stability transition, whereas a much broader downdip zone is inferred to be slipping in the natural events [*Dragert et al.*, 2001]. This discrepancy between model results and field measurements of SSEs suggested that we need to reevaluate the applicability of wet granite friction data in the subduction fault model, especially for the conditions under which slow slip events can take place.

[6] In this paper, we follow the approach of *Liu and Rice* [2007] to set up a 2-D Cascadia-like subduction fault model, with a zone of highly elevated pore pressure that is located using thermal, petrological and seismic constraints, and apply temperature-dependent rate and state friction data of wet granite [*Blanpied et al.*, 1998] and recently reported data for gabbro gouges [*He et al.*, 2007] to investigate, for each data set, conditions for aseismic slip and how the surface deformations produced by SSEs compare to geodetic measurements in northern Cascadia. We show that the application of appropriate experimental friction properties is of first-order importance for such forward models based on rate and state friction to produce results comparable to field observations.

[7] This paper is structured as follows. Section 2 introduces the rate and state friction law and the 2-D subduction fault model setup. Section 3 describes how friction parameter $a - b$ is constrained by experimental measurements of granite and gabbro gouges under hydrothermal conditions, and how other key parameters such as effective normal stress and characteristic evolution distance are constrained by seismological v_p/v_s observations, and by thermal and petrological models for the Cascadia and SW Japan subduction zones. Section 4 describes model results, based on the above two friction data sets, and comparisons to the GPS measurements of the 1999 episode in northern Cascadia as well as intertransient slip rate inferred from continuous GPS observations. Section 5 discusses fault dilatancy as a mechanism for generating slow slip events over a much larger range of velocity-weakening fault and its implication for the downdip limit of a megathrust earthquake rupture, potential 3-D effects and differences in using the ageing and slip state evolution laws.

2. Model Setup

2.1. Governing Equations

[8] We use the lab-derived rate- and state-dependent friction with a single state variable [e.g., *Dieterich*, 1979; *Ruina*, 1983]. Shear stress τ is dependent on the sliding velocity V and the state of asperity contacts, represented by state variable θ, on the frictional interface and is typically represented as

$$\tau = \bar{\sigma} f = \bar{\sigma}\left[f_0 + a \ln\left(\frac{V}{V_0}\right) + b \ln\left(\frac{V_0 \theta}{L}\right)\right], \qquad (1)$$

where f is the friction coefficient, L (also called d_c) is the characteristic slip distance for the renewal of asperity contacts population. To regularize that expression near $V = 0$, we actually use

$$\tau = a\bar{\sigma}\,\mathrm{arcsinh}\left[\frac{V}{2V_0}\exp\left(\frac{f_0 + b\ln(V_0\theta/L)}{a}\right)\right], \tag{2}$$

as justified by a thermally activated description of slip at frictional contacts [*Rice and Ben-Zion*, 1996; *Lapusta et al.*, 2000; *Rice et al.*, 2001], and which coincides very closely with it for essentially all states that arise in our simulations.

[9] For constant effective normal stress, two empirical evolution laws for state variable θ, which has the unit of time, have been commonly used. The ageing law

$$\frac{d\theta}{dt} = 1 - \frac{V\theta}{L} \tag{3}$$

better explains the laboratory observation that friction also evolves on stationary contacts (i.e., $V = 0$ [*Beeler et al.*, 1994]). The slip law

$$\frac{d\theta}{dt} = -\frac{V\theta}{L}\ln\frac{V\theta}{L} \tag{4}$$

predicts symmetric responses to velocity increases and decreases, and better represents the state evolution following large velocity jump tests [*Ruina*, 1983; *Bayart et al.*, 2006]. At steady state, $\theta = \theta_{ss} = L/V$, both evolution laws result in the same steady state friction $f_{ss} = f_0 + (a - b)\ln(V/V_0)$, where f_0 is a nominal friction coefficient at $V = V_0$. Using both ageing and slip laws, *Rubin* [2008] simulated slow slip events on a fault that is composed of completely locked, velocity weakening, velocity strengthening, and uniformly loaded (by imposed uniform slip rate) segments; fault lengths of the completely locked and uniformly loaded parts are much larger than those where rate and state friction applies. Self-sustained aseismic oscillations arise spontaneously within a smaller range of W/h^* for the slip law than for the ageing law. In the stable regime for both laws, the range of the maximum slip velocity is similar and the recurrence period and average slip of simulated SSEs are the same at a given W/h^*, for the same model geometry and friction parameter a/b distributions. The ageing evolution law is used for all the calculations in this paper. We expect modest variations in the SSE recurrence interval and amount of released slip from those using the slip law but they should not affect the main focus of this paper to compare the modeled surface deformation to GPS observations based on different friction data sets.

[10] The constitutive parameters a and b are interpreted in terms of the instantaneous change in f and the steady state f_{ss} in response to a velocity step: $a = V(\partial f/\partial V)_{inst}$ and $a - b = V(df_{ss}/dV)$. For $a - b > 0$, f_{ss} increases as velocity V increases. The surface is steady state velocity strengthening and sliding is stable. For $a - b < 0$, f_{ss} decreases as V increases. The surface is steady state velocity weakening and unstable sliding is possible when, for a single-degree-of-freedom spring-slider system governed by rate and state friction subject to small perturbations from steady sliding, the spring stiffness k is less than the system critical stiffness $k_{cr} = (b - a)\bar{\sigma}/L$. A critical nucleation size h^* can be defined by equating the single cell stiffness $k = 2\mu/\pi(1 - \nu)h$ (plain strain), for a fault segment of width h that is not too close to the surface, to k_{cr}. That is,

$$h^* = \frac{2\mu L}{\pi(1-\nu)(b-a)\bar{\sigma}}. \tag{5}$$

When applied to a subduction fault model, we use the average value $\langle b - a\rangle$ over a fault length where $a - b$ distribution with depth is not uniform in the definition of h^*. Shear modulus $\mu = 30$ GPa and Poisson's ratio $\nu = 0.25$.

[11] The rate and state friction law (equations (1)–(3)) is implemented together with the quasi-dynamic elastic relation between the distribution of shear stress and slip on the fault, with inclusion of a radiation damping term which is important only during seismic events [*Rice*, 1993; *Lapusta et al.*, 2000]. A detailed discussion of the elastic relation and its implementation in a thrust fault model is given by *Liu and Rice* [2005a].

2.2. Geometry

[12] The 2-D subduction fault model is set up similar to that of *Liu and Rice* [2007] and is summarized here in Figure 1. We simulate the thrust fault by a planar frictional interface in an elastic half-space, with the 2-D plane strain assumption such that properties are uniform along strike x (perpendicular to the y-z plane). As a simple representation of the northern Cascadia shallow subduction geometry, the thrust fault dips at a fixed angle of $\alpha = 12°$; ξ is along the downdip direction. Rate- and state-dependent friction is applied on the interface from the trench $\xi = 0$ to $\xi = W_0 =$ 300 km. Further downdip the fault is loaded by a constant plate convergent rate $V_{pl} = 37$ mm/a. Friction parameters a, $a - b$, L are functions of the downdip distance ξ, and are invariant with time. For simplicity, we only consider the elastic effect of slip on changing the shear stress, keeping the effective normal stress $\bar{\sigma}$ constant with time. Calculations that included the normal stress alteration due to slip on a 2-D thrust fault gave similar results [*Liu and Rice*, 2007].

[13] Such a 2-D model permits much higher numerical resolutions than 3-D, allowing the use of laboratory-based characteristic slip distances L (tens to hundreds of microns) for state evolution, and extensive exploration for model parameters that produce transients of recurrence intervals and cumulative slips similar to observations.

3. Constraints on Parameters and Application to the Model

3.1. Friction Parameter $a - b$

3.1.1. Granite

[14] Rate and state friction properties, including key parameters a, $a - b$ and L, are most systematically characterized in lab experiments for wet granite gouge [e.g., *Blanpied et al.*, 1991, 1995, 1998], and are most commonly adopted in theoretical and numerical studies of earthquake nucleation and earthquake cycles [e.g., *Rice*, 1993; *Kato and Hirasawa*, 1997; *Lapusta et al.*, 2000; *Lapusta and Rice*, 2003]. That includes our previous work on aseismic transients in subduction zones [*Liu and Rice*, 2005a, 2007], because nothing comparable was yet available for combinations of oceanic crust and subducted sediments. As shown

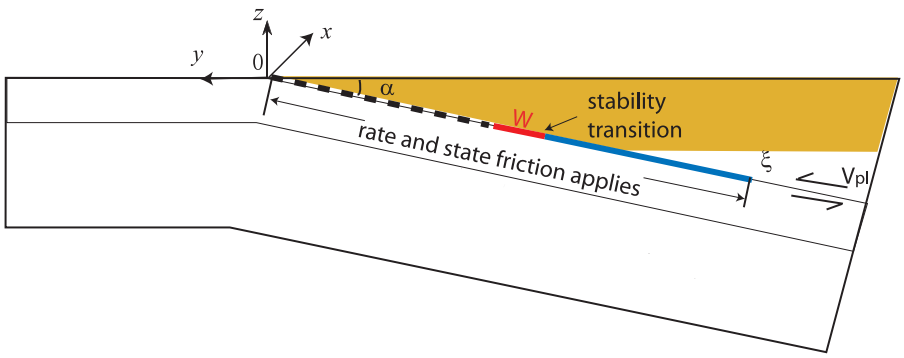

Figure 1. Two-dimensional subduction fault model. The thrust fault is simulated by a planar frictional interface dipping at $\alpha = 12°$ in an elastic half-space. The parameter ξ is distance along downdip direction. Rate and state friction applies from surface $\xi = 0$ to $\xi = W_0 = 300$ km, with depth-variable friction parameters. Fault is loaded by a constant plate rate $V_{pl} = 37$ mm/a downdip from $\xi = W_0$. Properties are uniform along the strike direction x (perpendicular to y-z plane). Bold red line represents the velocity-weakening fault of length W updip from the stability transition under low effective normal stress. Friction parameter $a - b$, effective normal stress $\bar{\sigma}$, and characteristic evolution distance L downdip distributions using wet granite and gabbro friction data are shown in Figures 3a and 3b, respectively.

in Figure 2a, the wet granite gouge data predict an upper friction stability transition from velocity strengthening ($a - b > 0$) to weakening ($a - b < 0$) at temperature $T \sim 100°$C and a lower stability transition from weakening to strengthening at $T \sim 350°$C. When we mention friction stability transition in this paper, we refer to the higher-T transition that is thought to correspond approximately to the temperature of the onset of quartz plasticity [*Scholz*, 2002]. Following *Tse and Rice* [1986], *Blanpied et al.* [1991] replotted their data as a function of crustal depth using a San Andreas Fault (SAF) geotherm [*Lachenbruch and Sass*, 1973] and found that the depth interval of small earthquakes, 1969–1988, on the central creeping section of the SAF corresponds very well to the interval of velocity weakening. Although granite is not a good proxy for the oceanic crust and subducted sediments, thermal models of several shallow subduction zones found the downdip limit of interseismic coupling, inferred from geodetic and paleogeodetic measurements, also corresponds to temperatures between 300°C to 400°C [e.g., *Hyndman and Wang*, 1995; *Currie et al.*, 2002; *Chlieh et al.*, 2008], leading to the hypothesis of thermally defined seismogenic zone of megathrust earthquakes. At temperatures above 350°C, experimental data show large scatter; the average $a - b$ at 600°C is of order 0.1. This implies a highly stabilizing velocity-strengthening zone, in contrast to $a - b \sim -0.004$ in the velocity-weakening zone. Such stabilizing effects may be a result of high-temperature chemical reactions between granite gouge and water, which probably become less or not relevant as aseismic transients are thought to occur at depth of active metamorphic dehydration, i.e., a water-repelling environment. In fact, at temperatures over 350°C, experiments on dry granite gouge show $a - b$ is approximately an order of magnitude smaller than its counterpart under wet conditions [*Stesky*, 1975; *Lockner and Byerlee*, 1986; *Chester and Higgs*, 1992; *Blanpied et al.*, 1995].

[15] The scattered $a - b$ versus T(°C) data in Figure 2a are approximated by several straight-line segments which have ends at (T, $a - b$) = (0, 0.004), (100, −0.004), (350, −0.004), (450, 0.045) and (500, 0.058), and mapped to be a function of the downdip distance as shown in Figure 3a using a Cascadia thermal model by *Peacock et al.* [2002]. The term $a - b$ starts at the trench as velocity strengthening but smaller than 0.004. This is because the temperature of the young subducting Cascadia slab at the trench is higher than 0°C. The velocity weakening to strengthening stability transition occurs at downdip ~66 km, and $a - b$ rapidly rises to larger than 0.04 downdip from 100 km. As shown in section 4, the shallow stability transition and highly stabilizing $a - b$ greatly influence the depth extent of modeled slow slip events and hence the comparison to GPS observations.

3.1.2. Gabbro

[16] Friction experimental data for gabbro, which is an essential part of the oceanic crust and chemically equivalent of basalt (a common mafic extrusive volcanic rock), under hydrothermal conditions have recently been reported by *He et al.* [2007]. Although the data are limited and highly scattered at some temperatures, we make tentative use of them as the first set available for a reasonable representation of the seafloor. As highlighted by a blue dashed line in Figure 2b, the velocity weakening to strengthening stability transition takes place at around 510°C under supercritical water conditions ($p_{H_2O} \geq 22$ MPa, $T \geq 374°$C). This is inferred from a set of data obtained under confining pressure 130 MPa, gouge pore pressure 30 MPa, and loading velocity steps between 0.244 and 0.0488 μm/s. These "slow" runs are more likely in a well "run-in" state (a long distance of long-term steady state (C. He, private communication, 2008)) and have loading velocities closer to tectonic rates, thus plausibly more representative of high-temperature gabbro friction properties than data from "standard" runs. At higher temperatures up to ~600°C, $a - b$ remains less than 0.01. The low level of velocity-strengthening $a - b$, compared to that of wet granite gouge, would allow aseismic slip, once nucleated around the stability transition, to propagate much further downdip. Gabbro friction data at lower temperatures in the velocity-weakening range show larger scatter, possibly due to different pressure conditions and limited slip distances.

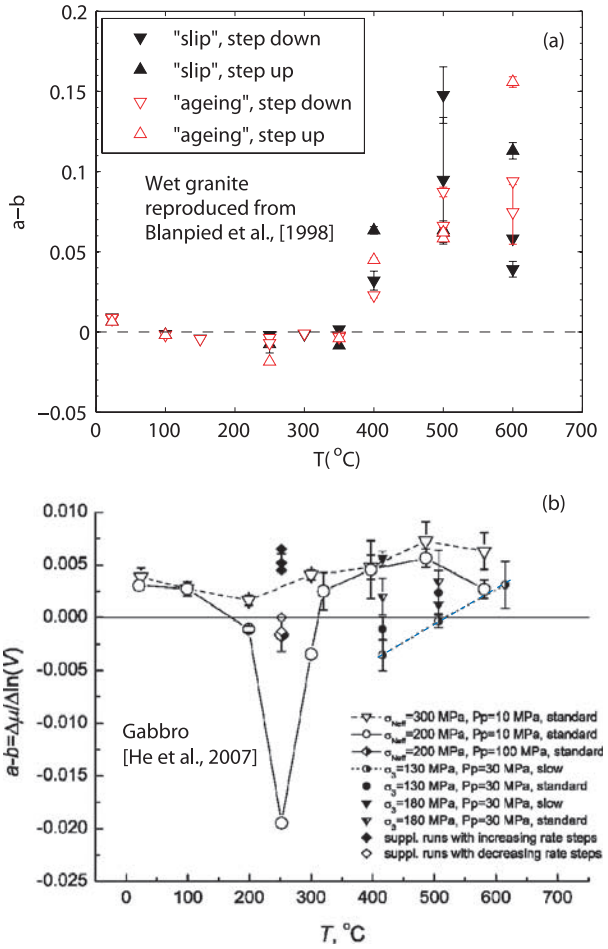

Figure 2. Friction parameter $a - b$ measured in laboratory fault-sliding experiments on granite and gabbro gouges under hydrothermal conditions. (a) Parameter $a - b$ reproduced from *Blanpied et al.* [1998] experiments on wet granite gouge, with constant normal stress 400 MPa and pore pressure 100 MPa. Black triangles represent parameters determined by inversion using the slip law for velocity step downs from 1 to 0.1 μm/s and velocity step ups from 0.1 to 1 μm/s. Red triangles represent parameters determined by inversion using the ageing law for velocity steps between 0.1 and 1 μm/s. (b) Temperature-dependent $a - b$ of gabbro gouge, from *He et al.* [2007]. In *He et al.*'s [2007] notation, σ_{Neff} is effective normal stress, P_p is fluid pressure, and σ_3 is confining pressure. We use p for fluid pressure and $\bar{\sigma}$ for effective normal stress in this paper. Standard denotes velocity steps between 1.22 and 0.122 μm/s, and slow denotes velocity steps between 0.244 and 0.0488 μm/s. Blue dashed line highlights the simplified (T, $a - b$) under supercritical water conditions used in modeling.

Such large uncertainties in the velocity-weakening data would certainly affect the rupture processes of megathrust earthquakes. But we expect negligible effects on the modeling of aseismic transients, because the latter, as shown in section 4, mostly take place near the stability transition at extremely low effective normal stress while the updip seismogenic zone is nearly locked at much higher $\bar{\sigma}$.

[17] The gabbro temperature-dependent friction data $a - b$ are approximated by straight-line segments that cover different stability regimes with ends at (T, $a - b$) = (0, 0.0035), (100, −0.0035), (416, −0.0035), (520, 0.001). Despite the large scatter in the velocity-weakening regime, we assume there $a - b$ to be a constant value of −0.0035, which is the lower bound of measurements at 416°C at supercritical water conditions. It is the approximately linear increase of $a - b$ from 416°C to 615°C, highlighted by the blue dashed line, that will mostly affect the outcome of aseismic slip patterns. Figure 3b shows the downdip distribution of $a - b$ with gabbro friction data. The term $a - b$ has similar values to the wet granite profile up to downdip ~60 km, where, instead of rising to the velocity-strengthening regime, it continues to be velocity weakening to ~95 km, followed by a gradual transition to velocity strengthening at ~180 km. The slow rise of $a - b$, thus a much wider transitional zone, is mainly attributed to the extremely small positive $a - b$ value at deeper part of the fault; $a - b$ is about 0.005 at the downdip end of the fault W_0 = 300 km.

[18] For both profiles, direct effect a is assumed to increase linearly with the absolute temperature: $a = 5.0 \times 10^{-5}(T + 273.15)$, following an Arrhenius activated process at asperity contacts on the sliding surface [*Rice et al.*, 2001]. The parameter a is also converted to be depth-dependent using the *Peacock et al.* [2002] geothermal profile for northern Cascadia.

3.2. Effective Normal Stress

[19] Effective normal stress $\bar{\sigma}$ is defined as the difference between the total lithostatic pressure σ and fluid pressure p within the fault gouge. The σ is assumed to increase linearly with depth z at the lithostatic gradient 28 [MPa/km]. In this paper, we use term "high fluid pressure" interchangeably with "low effective normal stress". The level of fluid pressure p is difficult to estimate, being a result of complicated processes such as overpressurization of sediments accompanying subduction, progressive fluid-releasing metamorphic reactions encountered by the oceanic crust at high pressure-temperature conditions, and slow permeation of fluids along and across the thrust fault. We try to constrain p as a function of depth (or, equivalently, along the downdip distance ξ) in the following way.

[20] First, near the surface and in most part of the seismogenic zone, we incorporate the elevated pore pressure concepts as discussed by *Rice* [1992] and assume p being the maximum between the hydrostatic pressure 10 [MPa/km] × z and $\sigma(z) - \bar{\sigma}_0$ = 28 [MPa/km] × $z - \bar{\sigma}_0$; $\bar{\sigma}_0$ is a constant level of effective normal stress at depth, usually taken in the range of 50 MPa to 150 MPa in crustal earthquake simulations [e.g., *Lapusta et al.*, 2000; *Lapusta and Rice*, 2003] and previous subduction earthquake simulations [*Liu and Rice*, 2005a, 2007]. In this paper, we take $\bar{\sigma}_0$ = 50 MPa for all simulation cases. This assumption of p results in a linear increase of $\bar{\sigma}$ from 0 at the surface to 50 MPa at z = 2.77 km (ξ = 13.36 km), followed by a plateau at 50 MPa, as shown in Figure 3 (middle).

[21] Recently, fluid pressure is suggested to be near-lithostatic at the source areas of episodic slow slip events and nonvolcanic tremors in subduction zones. Supporting evidence includes metamorphic dehydration reactions encountered as temperature and pressure increase in the

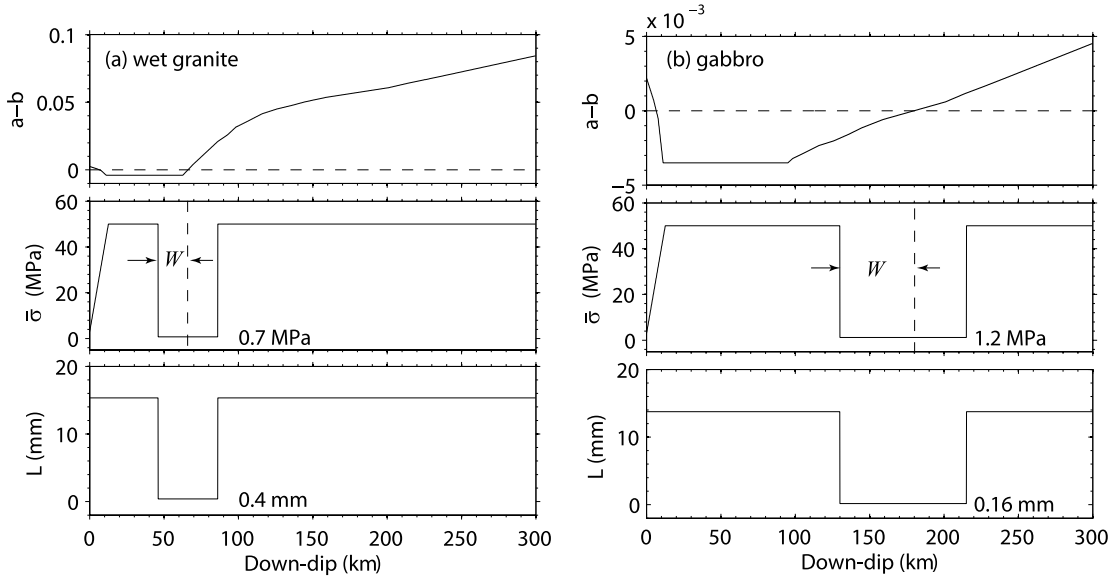

Figure 3. Downdip distributions of friction parameter $a - b$, effective normal stress $\bar{\sigma}$, and characteristic evolution distance L for models using (a) wet granite and (b) gabbro friction data. Temperature-dependent $a - b$ in Figure 2 are mapped to be depth-dependent using a Cascadia thermal model by *Peacock et al.* [2002]. Lower friction stability transition at ~66 and 180 km, respectively, is shown. W is the distance updip from stability transition with low $\bar{\sigma}$. Modeling results using the above sets of parameters are shown in Figures 5, 8, 10, and 12.

oceanic crust of shallow dipping subduction zones (e.g., Cascadia, SW Japan, southern Mexico) where short-period SSEs have been observed [*Peacock et al.*, 2002], seismological observations of high v_p/v_s and hence high Poisson's ratios along the plate interface in SW Japan and northern Cascadia subduction zones [*Kodaira et al.*, 2004; *Shelly et al.*, 2006; *Audet et al.*, 2009], and observations of tremors triggered by small stress perturbations of order 0.01 MPa due to teleseismic surface waves or tidal stressing [*Miyazawa and Mori*, 2006; *Rubinstein et al.*, 2007; *Gomberg et al.*, 2008; *Peng and Chao*, 2008; *Peng et al.*, 2008]. Numerical calculations also suggest fluid pressure is indeed extremely high at SSE and tremor sources. Using the slip model of *Dragert et al.* [2001], *Liu and Rice* [2007] found most of the tremor hypocenters located with the Source Scanning Algorithm [*Kao et al.*, 2006], that are widely distributed from 10 to 50 km in depth, coincide with positive but near zero (~0.01 MPa) "unclamping" stress changes induced by slow slip in northern Cascadia. In a recent tremor location study using S minus P time difference [*La Rocca et al.*, 2009], northern Cascadia tremors lie more closely along the subduction interface, similar to those in SW Japan. However, this does not affect the coincidence of tremors with small "unclamping" stress changes near the fault, which is an indication of low background effective normal stress.

[22] Seismic evidence for overpressured subducting oceanic crust and megathrust fault sealing is recently reported in northern Cascadia using converted teleseismic waves [*Audet et al.*, 2009]. Receiver function results showed a dipping, low-velocity layer beneath south Vancouver Island, for which the v_p/v_s and Poisson's ratios are estimated to be exceptionally high, indicating near-lithostatic fluid pressure in the oceanic crust. This implies that the plate interface probably represents a low-permeability boundary with water released from oceanic crust dehydration reactions capped within a subduction channel. The downdip limit of the low-permeability boundary may correspond to the eclogitization of the oceanic crust at about 45 km. However, the updip limit of the overpressured oceanic crust is unconstrained due to lack of offshore seismic observations. The ambiguity of tremor locations from different relocation techniques and absence of low-frequency earthquakes make it difficult to use tremors as a direct indicator of extremely high fluid pressure. We thus turn to a similarly young, warm and shallow dipping subduction zone, southwest Japan, where dense instrumentation such as Hi-net borehole stations facilitated the precise relocation of nonvolcanic tremors, including low-frequency earthquake signals, and velocity structures in the vicinity of the subduction slab. Our goal is first to find possible spatial correspondence between seismically inferred high fluid pressure zone and the depths of dehydration reactions accompanying major mineral phase changes on top and bottom of the subduction slab in SW Japan. We then draw an analogy to the northern Cascadia subduction zone, where such dehydration reaction depths can also be determined by its petrological and thermal structures, to estimate the distribution of fluid pressure along the subduction interface.

[23] For this purpose, we make a fuller use of the *Peacock et al.* [2002] phase diagram and thermal models [*Liu and Rice*, 2007, Figure 2] of northern Cascadia and SW Japan. We trace the thermal profiles of both subduction zones overlapped on the phase diagram, to identify the temperatures and pressures (equivalent to depths) where the top and bottom of the oceanic crust intersect the phase boundaries, respectively. The depth, temperature, and facies associated in these phase transitions are listed in Table 1 and

Table 1. Depth, Temperature, and Facies Involved in Phase Transitions on the Top and Bottom of the Northern Cascadia and SW Japan Subduction Slabs[a]

Slab	Depth (km)	Temperature (°C)	Phase Transition
	Northern Cascadia [*Peacock et al.*, 2002]		
Top	12.2	336.0	PA - GS
	29.6	468.7	GS → EB
	44.5	523.5	**EB → eclogite**
Bottom	21.1	538.0	AM → EA
	40.2	594.2	**EA → eclogite**
	SW Japan [*Peacock et al.*, 2002]		
Top	22.9	342.0	PA → GS
	26.6	375.0	GS → EB
	43.8	523.5	**EB → eclogite**
Bottom	30.5	490.0	GS → EA
	41.3	536.5	**EA → eclogite**
	Northern Cascadia [*Hacker et al.*, 2003; *Wada et al.*, 2008]		
Top	8.1	293.7	PP/PA → GS
	26.2	435.0	GS → EB
	42.6	505.0	**EB → eclogite**
Bottom	18.2	516.0	AM → EA
	36.0	561.3	**EA → eclogite**

[a]Based on the petrological and thermal models of *Peacock et al.* [2002], *Hacker et al.* [2003] and *Wada et al.* [2008]. Metamorphic facies are AM (amphibolite), EA (epidote amphibolite), EB (epidote blueschist), PP (prehnite-pumpellyite), PA (prehnite-actinolite), GS (greenschist). Phase transitions in bold fonts have the most water weight percent reductions.

also marked in Figure 4 (red for slab top; blue for slab bottom), assuming a dipping angle of 12° for northern Cascadia and 18° for SW Japan. The oceanic crust thickness is taken as 7 km for both. The most significant water-releasing phase transitions (in weight percent change) are epidote blueschist (EB) → eclogite on the slab top, and epidote amphibolite (EA) → eclogite on the slab bottom. Both transitions involve dehydration reactions which release ~1 to 2 weight % H_2O [*Hacker et al.*, 2003]. *Wada et al.* [2008] revised the Cascadia thermal model by including more realistic rheology in the mantle wedge. They found temperatures beneath the flowing part of the mantle are higher than that of *Peacock et al.* [2002], but effects on the shallower part are very small. On the basis of *Wada et al.* [2008]'s preferred Cascadia thermal profile overlapped on an updated phase diagram of oceanic crust [*Hacker et al.*, 2003], we found the major phase transitions (EB → eclogite and EA → eclogite) take place at similar depths and temperatures as predicted by *Peacock et al.* [2002] (Table 1). However, such a more sophisticated thermal model is currently not available for SW Japan due to insufficient heat flow data and complex slab geometry (I. Wada, private communication, 2008). We thus still use *Peacock et al.*'s [2002] results for both subduction zones.

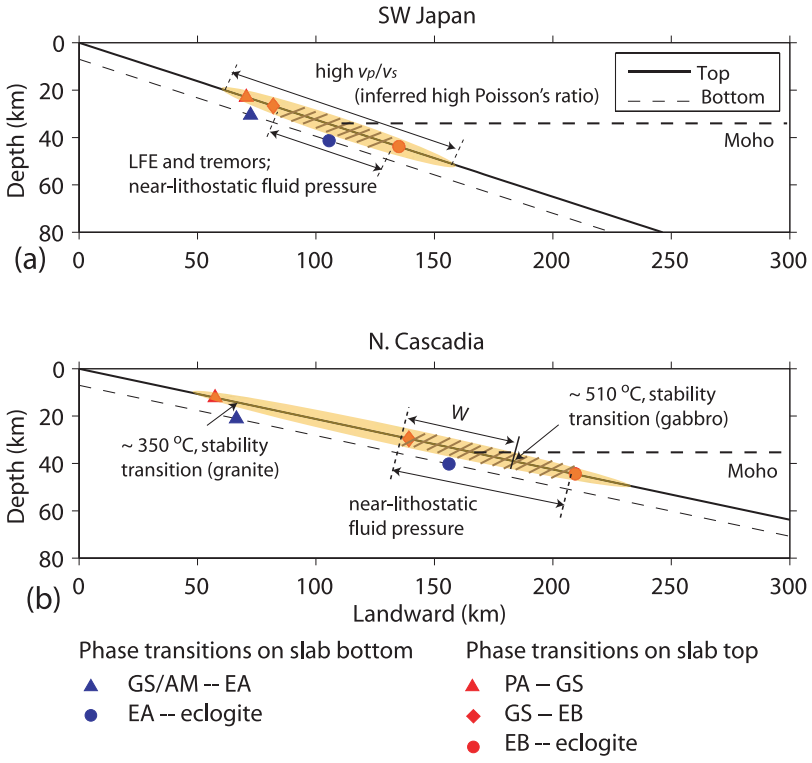

Figure 4. Schematic fluid pressure distribution on the subduction interface for SW Japan and northern Cascadia, based on petrological and thermal models of *Peacock et al.* [2002] and seismological observations of *Kodaira et al.* [2004], *Shelly et al.* [2006], and *Audet et al.* [2009]. Red and blue symbols represent major water-releasing phase transitions encountered by the top (solid) and bottom (dashed) of the subducting slab, respectively. See Table 1 for metamorphic facies abbreviations. Shaded yellow region represents generally high (overhydrostatic) fluid pressure p, and hatched lines represent depths of near-lithostatic p. In SW Japan, they correspond to the depth ranges of high v_p/v_s (and inferred high Poisson's ratio) and LFE/tremor locations, respectively. W is the distance updip from friction stability transition. The 510°C friction stability transition for gabbro gouge lies within the near-lithostatic p zone, while the 350°C transition for granite is much further updip.

[24] In SW Japan, seismological observations revealed high v_p/v_s beneath Shikoku [*Shelly et al.*, 2006] and a similarly inferred high Poisson's ratio in Tokai [*Kodaira et al.*, 2004] between 20 and 50 km along the subduction slab. Such properties suggest the existence of high fluid pressure, and may correspond to a generally overhydrostatic p level. This depth range is shaded in Figure 4a with yellow along the interface. Within this region, nonvolcanic tremors and low-frequency earthquakes are detected between 30 and 45 km [*Obara*, 2002; *Shelly et al.*, 2006], and may correspond to a near-lithostatic p level. This portion of the interface is highlighted with brown hatched lines. It is evident from Figure 4a that the major dehydration reactions in the subduction slab spatially correspond well with regions of generally overhydrostatic fluid pressure inferred from seismic studies. In particular, p may increase to a near-lithostatic level some distance updip from the slab bottom EA → eclogite transition, and returns to a lower, but overhydrostatic, level downdip from the EB → eclogite transition; dehydration released fluids would mostly permeate updip due to the density difference. We apply the above postulated spatial correspondence between fault interface fluid pressure and depths of major dehydration reactions, also determined from the petrological and thermal models of *Peacock et al.* [2002], to the northern Cascadia subduction zone, as shown in Figure 4b. The generally overhydrostatic fluid pressure zone, in light yellow shade, spans from depth ~10 to 50 km, corresponding to the range of dehydration phase transitions in the slab. This is also consistent with an overpressured oceanic crust from at least 20 km to 45 km in depth, implied by high v_p/v_s and Poisson's ratios from converted seismic waveforms beneath southern Vancouver Island [*Audet et al.*, 2009]. The near-lithostatic fluid pressure zone extends certain distance updip from the slab bottom EA → eclogite transition, and downdip to the vicinity of the slab top EB → eclogite transition at ~45 km. This depth range, highlighted with brown hatched lines, also approximately corresponds to nonvolcanic tremors within epicentral depth 30–45 km in northern Cascadia.

[25] We note from Figure 4 that for both subduction zones, based on the *Peacock et al.* [2002] thermal model, the ~510°C friction stability transition of gabbro gouge lies within the estimated near-lithostatic p region, while stability transition at ~350° for wet granite gouge is further updip outside of that region, especially for northern Cascadia. If we apply the estimated p distribution to a model using the wet granite friction data, the extremely low $\bar{\sigma}$ zone will be exclusively in the downdip velocity-strengthening region and no short-period (1–2 years) spontaneous aseismic transients can be produced. This inconsistency itself also suggests that wet granite friction data are not appropriate for modeling slow slip events in shallow subduction zones. Nevertheless, in order to compare model results to GPS measurements, we assume that, for the model using wet granite data, fluid pressure is near-lithostatic within certain distance updip and downdip from the stability transition around 350°C. One of such examples is shown in Figure 3a (middle), where effective normal stress is near zero (0.7 MPa) in a zone W = 20 km updip and downdip from the stability transition at ξ = 66 km. The parameter $\bar{\sigma}$ resumes to 50 MPa further downdip. For the model using gabbro friction data, we assume near-lithostatic fluid pressure in a region extending distance W updip from the ~510°C friction stability transition and about 35 km downdip to the depth of EB → eclogite transition. One example of $\bar{\sigma}$ downdip distribution is shown in Figure 3b (middle).

[26] As have been discussed by *Liu and Rice* [2007] and *Rubin* [2008],

$$\frac{W}{h^*} = \frac{W\pi(1-\nu)\langle b-a\rangle\bar{\sigma}}{2\mu L} \tag{6}$$

is an important parameter that determines whether the system can produce self-sustained aseismic oscillations. Here $\langle b-a\rangle$ is the average $b-a$ over W. For each friction profile (constant $a-b$ versus downdip distribution), model parameters W, low $\bar{\sigma}$ and L are related via equation (6). We first choose W that is in a reasonable agreement with the petrologically and seismologically estimated extent of the high-p region. That is a few tens of kilometers updip from the stability transition for the gabbro profile. For the wet granite profile, the choice of W is rather arbitrary as there is no constraint on p distribution near 350°C; W is taken between 10 and 30 km to reflect a moderate portion of the entire velocity-weakening zone. For each fixed W, the average $\langle b-a\rangle$ is thus determined. The parameters $\bar{\sigma}$ and L are then varied accordingly to result in a range of W/h^* that allow quasiperiodic slow slip events. On the rest of the fault, L is uniformly

$$L = \frac{\pi(1-\nu)(b-a)_{\max}h_0^*\bar{\sigma}}{2\mu}, \tag{7}$$

where $(b-a)_{max}$ = 0.004 (wet granite) or 0.0035 (gabbro) is the maximum velocity-weakening value, and h_0* is a fixed factor (16 in most calculations) times the computational grid size to assure reasonable freedom of computed results from grid discreteness effects.

[27] In the example shown in Figure 3a for wet granite, W = 20 km, L = 0.4 mm in the $\bar{\sigma}$ = 0.7 MPa zone such that W/h^* = 5. L = 15.34 mm on the rest of the fault. In Figure 3b for gabbro, W = 50 km, L = 0.16 mm in the $\bar{\sigma}$ = 1.2 MPa zone such that W/h^* = 15. Detailed model results based on the two sets of parameters are discussed in section 4.

4. Model Results

[28] For models using each friction data set, we first explore the parameter space to identify appropriate conditions that produce aseismic transients of cumulative slip δ and recurrence interval T_{cyc} similar to those observed in northern Cascadia, that is, slip 20–30 mm and period 1–2 years. Representative cases are then chosen to calculate the surface deformation, and compare to the GPS measurements.

4.1. Exploration of the Parameter Space

[29] A general fault response to the above loading and model parameter conditions is that megathrust earthquakes rupture the entire seismogenic zone every a few hundreds of years, and quasiperiodic aseismic transients, mostly limited within the low $\bar{\sigma}$ zone around stability transition, appear every a few years in the interseismic period. Figure 5 shows sequences of modeled aseismic transients within 50 years from the interseismic period, using the wet granite friction

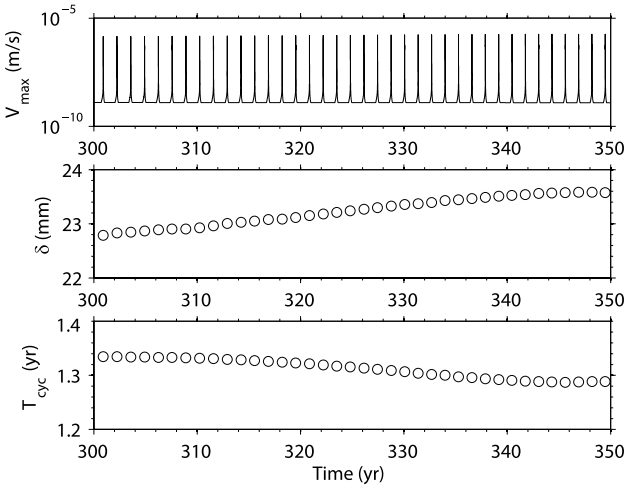

Figure 5. Short-period slow slip events in a 50-year interseismic period, using wet granite friction data. Model parameters are shown in Figure 3a. (top) Maximum slip rate. (middle) Cumulative slip at middle of velocity-weakening low $\bar{\sigma}$ zone when $V_{\max} > 2V_{pl}$. (bottom) Recurrence interval.

data. Model parameters are $W = 20$ km, $\bar{\sigma} = 0.7$ MPa and $L = 0.4$ mm, as in Figure 3a. Two megathrust earthquakes occur at ~84 and 410 years, with maximum slip velocity $V_{\max}$ about 1 m/s (not shown here). In the interseismic period, $V_{\max}$ oscillates between V_{pl} and the peak aseismic rate of $\sim 10^{-6}$ m/s. Figure 5 (middle) shows slip δ at the center of velocity-weakening low $\bar{\sigma}$ zone accumulated during each episode of transient slip when $V_{\max}$ exceeds $2V_{pl}$. The parameter δ fluctuates slightly from event to event with an average of ~22.8 mm. Different velocity thresholds to determine the onset and turnoff of transient slip can result in slightly different δ. For example, if the velocity threshold changes from $2V_{pl}$ to $1.5V_{pl}$, the average δ increases to 23.2 mm. This does not affect the general results shown in Figure 6. Figure 5 (bottom) shows the recurrence period T_{cyc}, defined as the interval between two successive events when $V_{\max}$ reaches the peak value around 10^{-6} m/s. The small variations in δ and T_{cyc} are due to the interseismic strength evolution in the transitional zone and updip in the nearly locked seismogenic zone. It is consistent with the observation that natural episodes of slow slip events in a subduction zone also exhibit some degree of variation in magnitude and recurrence interval with time. To select δ and T_{cyc} representative of the interseismic period, we choose events with $V_{\max}$ peaks that are relatively constant and $V_{\max}$ minimum at V_{pl} (to exclude earthquake nucleation and postseismic relaxation periods). Multiple time windows, which usually contain more than 100 events, are selected for each simulation case. We then make the histograms of selected δ and T_{cyc}, identify their maximum likelihood values, and record the minimum and maximum of each property as its variation range.

[30] While the coseismic slip and recurrence interval of megathrust earthquakes are relatively invariant due to the constant $\bar{\sigma} = 50$ MPa and $L = 15.34$ mm in most of the seismogenic zone, slip δ and period T_{cyc} of aseismic transients vary significantly for a wide range of choices of W, lower level $\bar{\sigma}$ and L. Four groups of calculations with $W =$ 10, 15, 20 and 30 km using wet granite data are summarized in Figure 6. For each group of a given W, $\bar{\sigma}$ and L are varied according to equation (6) to result in $W/h^* = 3, 4, 5$ .. until seismic instability. Aseismic slip δ, recurrence period T_{cyc} and maximum velocity $V_{\max}$ are plotted versus W/h^*: symbols and error bars represent the maximum likelihood values and variations, respectively. The lower limit of W/h^* for the onset of spontaneous aseismic transients is around 2, where the maximum velocity is around $10V_{pl}$. $V_{\max} \sim 10^5 V_{pl}$ $\sim$ 0.1 mm/s at $W/h^* = 7$; seismic instability is expected for larger choices of W/h^*. The scaling of δ and T_{cyc} with L makes it possible to label the axes so that the solutions can be interpreted for different L. For example, $\delta \approx 23$ mm and $T_{cyc} \approx 1.3$ years for $L = 0.4$ mm at $W/h^* = 5$ can also be interpreted as $\delta \approx 46$ mm and $T_{cyc} \approx 2.6$ years for $L = 0.8$ mm

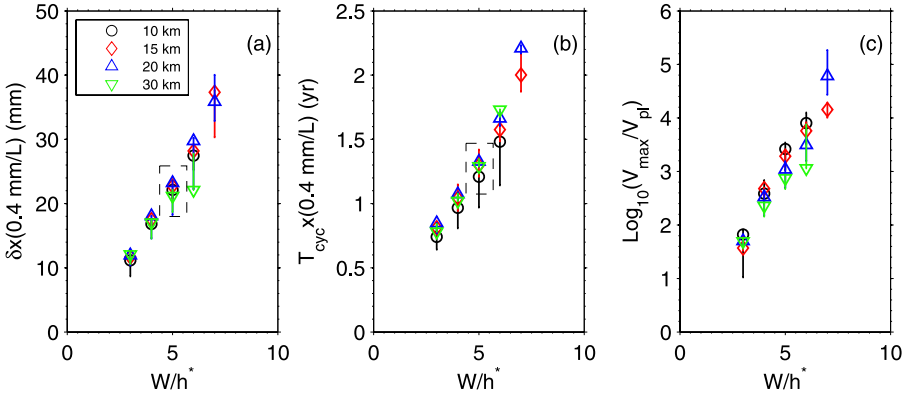

Figure 6. Exploration in the parameter space, using wet granite friction data, shows that modeled SSE (a) cumulative slip, (b) recurrence interval, and (c) maximum velocity all increase with W/h^*. Simulation cases using $W = 10$, 15, 20, and 30 km are shown in black, red, blue, and green symbols, respectively. Small variations in δ and T_{cyc}, as shown in Figure 5, for each case are represented by error bars. $L =$ 0.4 mm is used in most simulations, but δ and T_{cyc} can also be interpreted for other choices of L by the scaling labeled on their axes. Dashed line box highlight calculations with slip and period similar northern Cascadia observations, using $L = 0.4$ mm.

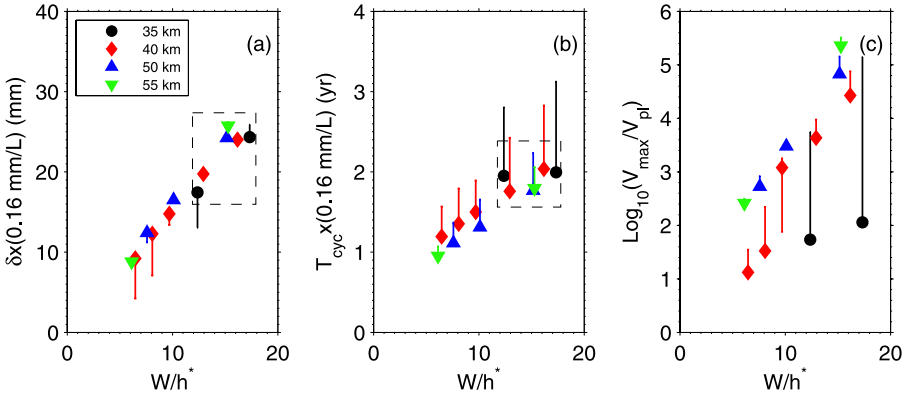

Figure 7. Exploration in the parameter space, using gabbro friction data, shows that modeled SSE (a) cumulative slip, (b) recurrence interval, and (c) maximum velocity all increase with W/h^*. Simulation cases using W = 35, 40, 50, and 55 km are shown in black, red, blue, and green symbols, respectively. The maximum likelihood value and variations in δ and T_{cyc} for each simulation case are represented by the solid symbols and error bars, respectively. L = 0.16 mm is used in the scaling, but δ and T_{cyc} can also be interpreted for other choices of L. Dashed line box highlight calculations with slip and period similar northern Cascadia observations, using L = 0.16 mm.

at the same W/h^*. Slip δ appears to increase linearly with W/h^*, despite the small variations in using different W. This is also observed by *Rubin* [2008] for simple periodic events in a 2-D subduction fault model with most of the seismogenic zone completely locked. Different friction parameters a and $a - b$ are used by *Rubin* [2008]. Variations in all three properties among different W groups are very small, possibly due to the fact that $a - b$ is almost uniformly -0.004 within W except the linear increase to zero over a short downdip distance of 3.5 km ($\ll W$).

[31] The effect of depth-variable friction parameters on modeled slow slip events is further demonstrated in Figure 7, where gabbro friction data are used. Three basic properties of modeled slow slip events, δ, T_{cyc} and $V_{\max}$, are plotted versus W/h^* for four groups of length W. There are two main reasons for our limited choices of W = 35, 40, 50 and 55 km. First, W less than ~35 km or larger than ~55 km would imply a too narrow or too wide near-lithostatic fluid pressure zone that is inconsistent with our conjecture based on available seismological observations and petrological and thermal models discussed in section 3. Second, in some cases with W = 30 km, aseismic transients appear only for a short period after megathrust earthquakes and the oscillation quickly decays with time, resulting in a too small sample of transients to statistically identify δ and T_{cyc}. Spontaneous aseismic transients arise between $W/h^* \sim 6$ to 16; $V_{\max} \sim$ 0.3 mm/s at $W/h^* = 15.3$. Variations in the three properties with different W are larger than those for the wet granite model, because the velocity-weakening $a - b$ follows a gradual increase to neutral stability over the entire length of W. Significant variations in moment rate and maximum velocity are also reported by *Rubin* [2008] for models using linear gradients of a/b to approach neutral stability, compared to models with an abrupt change from $a/b < 1$ to $a/b > 1$. The particularly large range in $V_{\max}$ for W = 35 km is also due to a collection of high speed transients ($V_{\max} \sim 10^{-4}$ m/s) following a megathrust earthquake (but after postseismic relaxation) and low-speed transients ($V_{\max} \sim 10^{-7}$ m/s) later in the interseismic period. The low speed events are usually more populous than high-speed ones, thus the maximum likelihood value at the lower end. As W decreases to 30 km, most of the interseismic period becomes free of transients. A different scaling of 0.16 mm/L is applied on the axes of δ and T_{cyc} so that they are centered around slip of ~20 mm and period of 1 to 2 years. Slip δ also appears to linearly increase with W/h^*. On a log-log scale, the recurrence interval approximately follows a scaling relation $V_{pl}T_{cyc}/L \propto (W/h^*)^{0.7} \propto (\bar{\sigma}H/\mu L)^{0.7}$, where $H = W_0\sin(\alpha)$ is the vertical dimension of the simulated fault region. Note that an exponent of 0.4 was typical in our earlier simulation cases of simple periodic transients with a completely locked seismogenic zone using the wet granite friction data with *Fluck et al.* [1997] thermal model of Cascadia [Liu and Rice 2007, equation (7)]. The difference in the exponent is mainly due to the unlocked seismogenic zone and the dramatically different gabbro friction data used in the current model. Since the transients are quasiperiodic, we do not attempt to generalize the scaling of T_{cyc} with $\bar{\sigma}$ as in the work by *Liu and Rice* [2007].

[32] Figures 6 and 7 summarize three important properties of aseismic transients that such models can produce, among which slip and recurrence period can be relatively accurately determined from geodetic observations. For the assumed a and $a - b$ downdip distributions, on the one hand, the exploration in parameter space allows us to identify sets of parameters W, $\bar{\sigma}$ and L that produce similar solutions. On the other hand, given estimates of the above parameters, we can determine whether they would lead to spontaneous transients, and furthermore estimate the total aseismic slip and recurrence period. Dashed line boxes in Figures 6 and 7 highlight such simulation cases that generate transients of slip 20–30 mm and period 1–2 years, for the assumed scaling with L. Using the wet granite friction data, model with W = 20 km, $\bar{\sigma}$ = 0.7 MPa and L = 0.4 mm produce transients of slip ~23 mm and period ~1.3 years. Using the gabbro data, model with W = 50 km, L = 0.16 mm and $\bar{\sigma}$ = 2 MPa generates transients of slip ~24 mm and period ~2 years. Other sets of parameters can

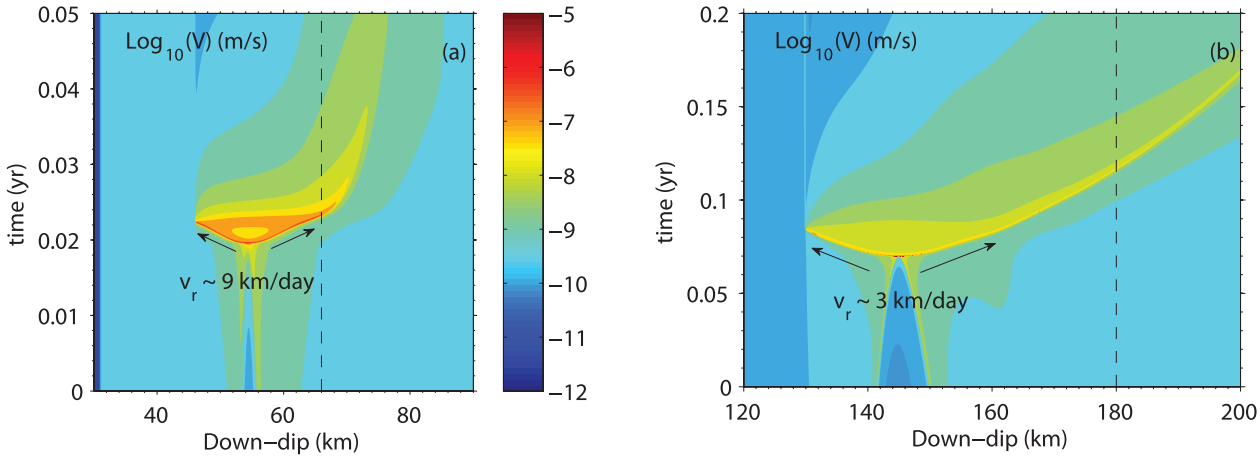

Figure 8. Slip velocity history during one transient event, using (a) wet granite (parameters in Figure 3a), and (b) gabbro (parameters in Figure 3b) friction data sets. The term $\log_{10}(V)$ in m/s is contoured. For reference, V_{pl} = 37 mm/a $\approx 1.2 \times 10^{-9}$ m/s. Vertical dashed line plots the position of friction stability transitions. For wet granite profile, low $\bar{\sigma}$ zone is from 46 to 86 km. For gabbro profile, low $\bar{\sigma}$ zone from is 130 to 215 km. Arrows show the along-dip bilateral slip propagation directions. The parameter v_r is the estimated propagation speed.

also result in similar amount of slip and recurrence interval, with $V_{\max}$ in the range of 10 to 10^5 times V_{pl}. These two examples are selected such that the characteristic slip distance L in the low $\bar{\sigma}$ zone gets close to lab values yet calculations can be done in reasonable durations. They will be used in sections 4.2 and 4.3 to illustrate the transient slip history and comparisons to GPS measurements.

4.2. Transient Slip Velocity Evolution

[33] Figures 8a and 8b illustrate the slip velocity history during modeled transient events, using wet granite and gabbro friction data set, respectively. Downdip distributions of parameters are shown in Figure 3 for each model. For reference, the plate convergence rate is V_{pl} = 37 mm/a $\approx 1.2 \times 10^{-9}$ m/s. Only the depth range involved in the transient slip is plotted. For the wet granite profile, the friction stability transition is at downdip 66 km, and the low $\bar{\sigma}$ zone from 46 to 86 km. For the gabbro profile, the stability transition is at downdip 180 km, and the low $\bar{\sigma}$ zone from 130 to 215 km. In both models, two nucleation fronts slowly march toward each other within the velocity-weakening zone low $\bar{\sigma}$ zone, before they merge and reach the maximum slip velocity. Slip then propagates in both updip and downdip directions along the fault. The updip propagation continues at a relatively constant speed until it encounters the abrupt increase to high $\bar{\sigma}$ = 50 MPa. Downdip propagation speed in the wet granite model is comparable to the updip speed before it reaches the stability transition, further downdip from which the propagation speed is rapidly reduced due to the increase of $a - b$ to velocity strengthening over a short distance. Following the maximum velocities in respective slip marching fronts, we estimate the slip propagation speed v_r to be about 9 km/d in the velocity-weakening zone. The entire process when slip rate is higher than $10^2 V_{pl}$ is less than 0.01 year, or about 3 days. The downdip propagation in the gabbro model gradually slows down as $a - b$ increases toward velocity strengthening over a relatively long distance. Nevertheless, v_r for the first 20 km propagation is about 3 km/d in both updip and downdip directions. Similar along-strike slip propagation speeds are expected in a 3-D simulation with the same parameters and model resolution. Slip velocity continues to be higher than V_{pl} for about 0.1 year, but the moment is mostly released in less than 0.05 year, or about 15 days. In addition to the differences in slip propagation speed and event duration, we also note that for the gabbro model after a maximum slip velocity of 1.6×10^{-4} m/s is reached at the center of transient nucleation zone at $t \sim 0.07$ year, slip velocity quickly falls to between 10^{-7} and 10^{-6} m/s along the propagating fronts. For the wet granite model, a maximum slip velocity of 1.8×10^{-6} m/s is also reached at the center of nucleation zone. However, the propagating fronts continue to slip at high velocities between 10^{-7} and 10^{-6} m/s, before they encounter the barriers of high effective normal stress or friction stability transition.

4.3. Comparison to GPS

[34] An example of transient and intertransient slip downdip distributions in a 5-year time window, using the wet granite friction data, is shown in Figure 9a. Four episodes of transients are included, each releasing a maximum slip of about 23 mm in the velocity-weakening low $\bar{\sigma}$ zone. Much smaller slip takes place in the downdip velocity-strengthening region. Intertransient slip rate is calculated as an average rate during the period between sampled transients when $V_{\max}$ on the fault is V_{pl}. Transient slip is recorded as the cumulative slip on the fault when $V_{\max}$ exceeds $2V_{pl}$. This would include the transient nucleation phase and posttransient relaxation, and, for the wet granite profile, corresponds to the slip (gaps in Figure 9a) released in about 0.1 year, a duration twice of that shown in Figure 8. However, more than 90% of slip is released during the high-velocity period in Figure 8.

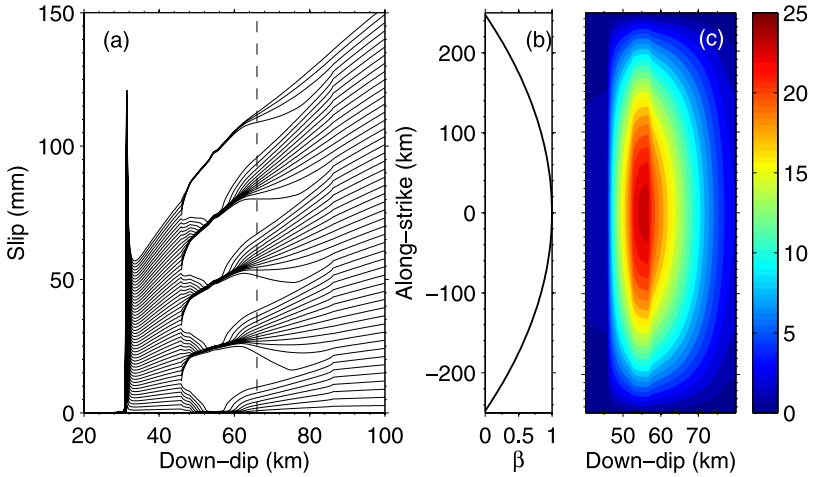

Figure 9. (a) Cumulative slip in a 5-year window, including four episodes of SSEs, using wet granite friction. Slip lines are plotted every 0.1 year. Vertical dashed line denotes the friction stability transition. During each SSE, maximum slip of about 23 mm is released in the velocity-weakening low $\bar{\sigma}$ zone, with much smaller slip in the downdip velocity-strengthening zone. Peak at ~30 km corresponds to the nucleation front for the next megathrust earthquake. (b) Along-strike distribution function $\beta(x) = 4(1/2 - x/L_{strike})(1/2 + x/L_{strike})$; x is along-strike distance, from −250 to 250 km, and L_{strike} = 500 km. (c) Extrapolated 3-D transient slip (mm), based on the 2-D distribution in Figure 9a and multiplied by $\beta(x)$.

[35] To calculate surface deformation, we extrapolate the 2-D transient slip and intertransient slip rate, which are variables of the downdip distance, to 3-D distributions, assuming both follow an along-strike profile function $\beta = 4(1/2 - x/L_{strike})(1/2 + x/L_{strike})$. Here L_{strike} = 500 km is the approximate along-strike fault length that is affected during slow slip events in northern Cascadia, and x varies between $-L_{strike}/2$ and $L_{strike}/2$. The parameter β is at maximum of 1.0 at the center x = 0 and decreases along strike to 0 at each edge (Figure 9b). The extrapolated 3-D transient slip distribution, using the wet granite friction data, is shown in Figure 9c.

[36] The northern Cascadia trench is simplified by a straight line oriented 34.16° NNW, as an approximation to the Juan de Fuca and North American plate boundary (Figure 10). The fault along-strike center is aligned with GPS station PGC5 in the direction perpendicular to the simplified trench line. *Okada*'s [1992] solution for dislocations in an elastic half-space is used to calculate the surface deformation and deformation rate due to the extrapolated transient slip and intertransient slip rate on the fault.

[37] Here, GPS measurements of intertransient deformation rate are analyzed by *McCaffrey* [2009] for permanent stations ALBH, NANO, NEAH, SEAT, SEDR and UCLU, where nine episodes of slow slip events have been reported from continuous observations for more than one decade. For station PGC5 that is not included in the *McCaffrey* [2009] analysis, we approximate the intertransient deformation rates as their 6.6-year average secular velocities [*Mazzotti et al.*, 2003] multiplied by a factor of 1.6, which is estimated based on other stations where both types of deformation rates are available. For example, the ratio between the intertransient and secular velocities at station ALBH is also about 1.6 [*Dragert et al.*, 2004]. GPS measurements of transient deformation are from observations of the 1999 slow slip event in northern Cascadia [*Dragert et al.*, 2001], with intertransient motion removed assuming an event duration of 15 days at each station.

4.3.1. Wet Granite

[38] Using wet granite friction data, the extrapolated 3-D distribution of intertransient slip rate, with V_{pl} removed, is projected on the surface in Figure 10a. Detailed model parameters are in Figure 3a. The firmly locked fault segment near the surface (dark color) is consistent with the complete interseismic locking at the shallow ~60 km inferred from leveling lines and tide gauge data in northern Cascadia [*Hyndman and Wang*, 1995]. However, the wet granite friction model predicts an abrupt change from complete locking to nearly free slipping at downdip ~60 km (sudden change from dark to light color), while the *Hyndman and Wang* [1995] model requires slip rate on the following ~60 km of fault segment to linearly increase from 0 to V_{pl}, in order to better explain the long-term geodetic data. As a result, the predicted intertransient surface deformation rate (horizontal component shown here) only agrees reasonably well with GPS observations at two coastal stations but cannot explain signals at most of the inland stations. Cumulative aseismic slip is projected on the surface as shown in Figure 10b. Slip of more than 20 mm concentrate in a relatively narrow along-dip region, corresponding mostly to the assumed low $\bar{\sigma}$ zone updip from the friction stability transition. Modeled deformation again can only explain observations at the coastal stations, but fails to match those at stations further away from the trench.

[39] To quantify the comparison between observed and modeled deformation and deformation rate, we define a misfit function

$$\chi^2 = \frac{1}{N}\sum_{i=1}^{N}\frac{\left(\vec{x}_i^{cal} - \vec{x}_i^{obs}\right)^2}{\vec{\sigma}_i^2}, \tag{8}$$

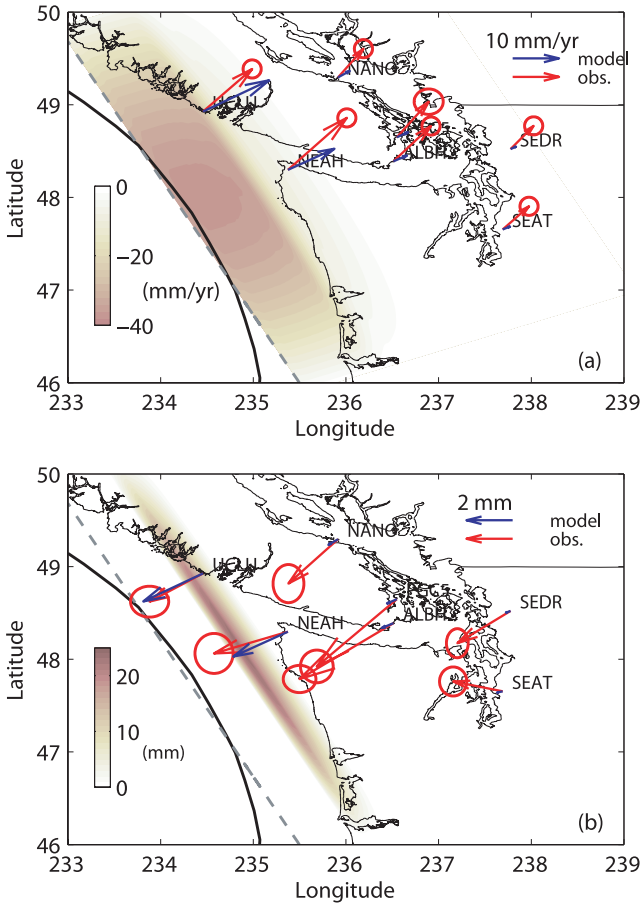

Figure 10. Comparison between observed (red arrows) and model predicted (blue arrows) intertransient deformation rate and transient deformation, using the wet granite friction data. Model parameters are shown in Figure 3a. (a) Intertransient slip rate, with V_{pl} = 37 mm/a removed, projected on the surface. Along-strike center aligned with station PGC5 is perpendicular to the simplified straight trench line (dashed). Dark colors represent strong interseismic locking, and light colors represent transition to free sliding at V_{pl}. Error ellipses are double the 95% confidence limits derived from regression errors [*Mazzotti et al.*, 2003; *McCaffrey*, 2009]. (b) Transient slip, with intertransient slip removed, projected on the surface. Error ellipses are double the 95% confidence limits reported by *Dragert et al.* [2001]. Error contribution from the intertransient slip rate is negligible compared that from transient slip because of the assumed short event duration of 15 days at each station.

where $\vec{x}_i^{cal}$ and $\vec{x}_i^{obs}$ are model predicted and observed horizontal displacement vectors, and $\vec{\sigma}_i$ is the standard derivation at the ith station. Total station number $N = 7$. For the case shown in Figure 10, transient deformation misfit is χ^2_{tran} = 127.6 and intertransient deformation rate misfit is χ^2_{inter} = 76.6. Similar cumulative aseismic slip and recurrence period are produced using W = 30 km, $\bar{\sigma}$ = 0.45 MPa and L = 0.4 mm (W/h^* = 5; see Figure 6). When the model results are compared to GPS measurements, the misfit functions are χ^2_{tran} = 125.7 and χ^2_{inter} = 73.0. We expect simulations from other groups of W using the wet granite data will have even larger misfits as the slip area remains shallow but narrower.

4.3.2. Gabbro

[40] A group of simulation cases that produce transients of slip 20–30 mm and recurrence period of ~2 years are listed in Table 2, corresponding to cases in the dashed line boxes in Figure 7. W/h^* ranges from 12.4 to 17.3, due to different sets of W and $\bar{\sigma}$; L is uniformly 0.16 mm in all cases. The parameter δ_{max} is the maximum cumulative aseismic slip on the fault. The parameter δ_{max} is usually located at the center of the slip nucleation zone, where velocity reaches maximum as shown in Figure 8. Among the listed cases, misfit function χ^2_{tran} is smallest for case e: W = 50 km, $\bar{\sigma}$ = 1.2 MPa and L = 0.16 mm. However, the limited number of simulation cases does not guarantee this is the best fitting model using the gabbro friction data. For each set of W and W/h^* ($\bar{\sigma}/L$ is thus determined), the linear scaling of δ with L allows us to calculate χ^2_{tran} for a suite of transient slip downdip distributions $\delta(\xi)$ without actually performing the earthquake and slow slip sequences simulations. For example, we expect that, with W = 35 km, W/h^* = 12.4 and $\bar{\sigma}$ = 4 MPa (thus L = 0.32 mm), $\delta(\xi)$ is just twice of the slip on the fault from model a, with δ_{max} = 36.8 mm. The recurrence period also becomes twice longer of that from model a. The term χ^2_{tran} = 35.0 for the new distribution $\delta(\xi)$. Each curve in Figure 11 is calculated based on such scaling relation for the same W and W/h^*. For models with the same W but different W/h^* (e.g., a and b, c and d), the χ^2_{tran} versus δ_{max} curves are very close to each other with similar minimum. For W = 35 km (black lines), the minimum χ^2_{tran} is reached at $\delta_{max} \sim 40$ mm. This implies a recurrence period between 3.2 and 4.3 years, which is much longer than the observed interval in Cascadia, suggesting that W = 35 km is not a good estimate of the fault length of the velocity-weakening low $\bar{\sigma}$ zone in order to fit the transient surface deformation. It is clear that models with W = 40 km cannot best fit the observations either. Both models e and f have χ^2_{tran} near the minimum values, with δ_{max} about 25 mm and recurrence period about 1.75 years and can be considered as best fitting models for the transient slip.

[41] The extrapolated 3-D distribution of intertransient slip rate and transient slip based on model e are projected on the surface in Figures 12a and 12b, respectively. Detailed model parameters are in Figure 3b. The downdip end of

Table 2. Model Cases Using the Gabbro Friction Data[a]

Model	W (km)	$\bar{\sigma}$ (MPa)	L (mm)	W/h^*	δ_{max} (mm)	χ^2_{tran}	χ^2_{inter}
a	35	2.0	0.16	12.4	18.4	79.2	141.8
b	35	2.8	0.16	17.3	24.7	55.5	151.4
c	40	1.6	0.16	12.9	20.0	53.5	147.9
d	40	2.0	0.16	16.2	24.6	37.4	145.7
e	50	1.2	0.16	15.2	24.1	22.7	142.2
f	55	1.0	0.16	15.3	25.8	23.5	143.5

[a]With different parameter sets of W, $\bar{\sigma}$, and L that produce episodic aseismic slip between 18 and 25 mm and recurrence period between 1 and 2 years. The parameter δ_{max} is the maximum accumulated slip on the fault, located at the center of the slip nucleation zone, where maximum velocity is reached (Figure 8). Misfit χ^2_{tran} is smallest for model e: W = 50 km, $\bar{\sigma}$ = 1.2 MPa, and L = 0.16 mm. Intertransient slip rate misfit is uniformly large for all model cases.

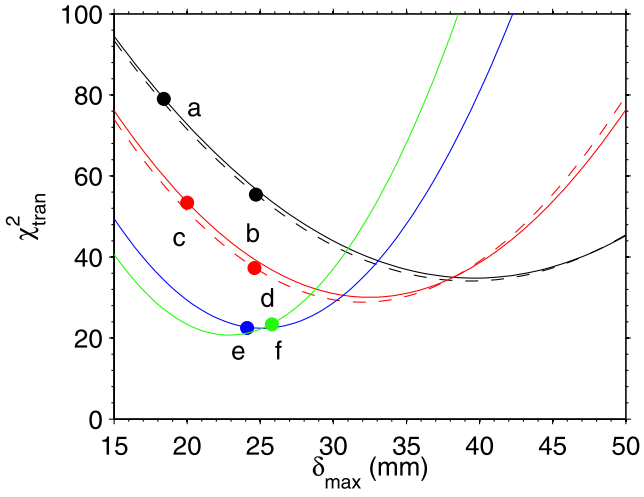

Figure 11. Dependence of χ^2_{tran} on modeled aseismic slip δ_{max}. Each curve is calculated based on the scaling between slip downdip distribution $\delta(\xi)$ and L and the linear relation between surface deformation and $\delta(\xi)$, for fixed W and W/h^*. Black indicates W = 35 km, W/h^* = 12.4 (solid) and 17.3 (dashed). Red indicates W = 40 km, W/h^* = 12.9 (solid) and 16.2 (dashed). Blue indicates W = 50 km, W/h^* = 15.2. Green indicates W = 55 km, W/h^* = 15.3. Models a–f listed in Table 2 are also plotted as individual dots on the curves.

complete interseismic locking extends to ~100 km from the trench, followed by a gradual transition to stable sliding near V_{pl} at ~200 km downdip distance. The locked and transitional slip fault lengths are larger than those inferred from long-term geodetic data [*Hyndman and Wang*, 1995] and are primarily responsible for the overprediction of the short-term intertransient deformation rate as shown in Figure 12a. The depth of complete interseismic locking is mainly determined by the distribution of $a - b$ in the seismogenic zone, which, for gabbro because of the large scatter in measurements at 250°C, we assume to be a constant of −0.0035 up to T = 416°C (corresponding to downdip ~95 km) at supercritical water conditions. Future laboratory experiments on gabbro friction properties at intermediate temperatures should help to better constrain the depth of interseismic locking. Aseismic slip of more than 20 mm are distributed within the ~80 km along-dip low $\bar{\sigma}$ zone, which is much further inland than the model using wet granite data. The comparison to GPS measurements of transient deformation is significantly improved at most stations.

[42] The simple planar fault model presented in this paper does not take into consideration any geometry variations along the trench or with depth, while 3-D subduction slab models [*Fluck et al.*, 1997] do suggest slab curvatures beneath the southern Vancouver Island. Depth contours of the plate interface approximately follows the orientation of the trench (thick black line). This partly explains the large discrepancies in transient deformation comparison at stations that are far from the center of the slip area, e.g., UCLU and SEAT. Incorporation of a more realistic fault geometry should reduce the discrepancies at those stations. For instance, if the slip area shown in Figure 12b follows the curved trench line, model predicted displacement would improve at station UCLU and reduce at SEAT. Another uncertainty is that in using *Okada*'s [1992] solution to calculate surface deformation we do not consider the spatial variations in the elastic properties of the lithosphere. Instead, constant shear modulus of 30 GPa and Poisson's ratio of 0.25 have been used, while seismic reflection imaging in northern Cascadia reveals complex regional structures beneath the Vancouver Island [*Calvert*, 2004].

5. Discussion

5.1. Wet Granite and Gabbro Friction Data and Implication for Downdip Limit of Seismogenesis

[43] Previous studies on modeling episodic slow slip events [*Shibazaki and Iio*, 2003; *Liu and Rice*, 2005a, 2007; *Shibazaki and Shimamoto*, 2007; *Rubin*, 2008] showed that aseismic transients emerge as a natural outcome of the laboratory-revealed rate and state friction processes at certain depth-variable friction parameter and effective normal stress distributions. Numerical models can produce features, such as the average velocity, cumulative aseismic slip and recurrence interval, qualitatively similar to those

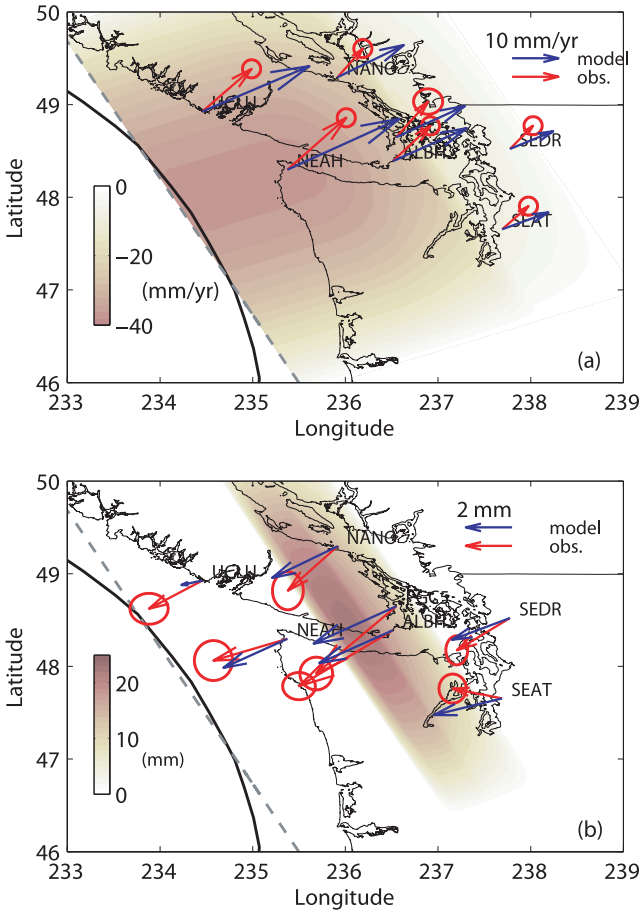

Figure 12. Comparison between observed (red arrows) and model predicted (blue arrows) intertransient deformation rate and transient deformation, using the gabbro friction data. Model parameters are shown in Figure 3b. (a) Intertransient slip rate and (b) transient slip. See Figure 10 caption for details.

inferred for natural events. However, no comparison between model predicted and geodetically observed (by GPS at most subduction zones) transient deformation has yet been made. A large uncertainty in attempts to compare these two is our limited knowledge of appropriate friction properties to use in the subduction fault models. Friction data, in particular, the temperature-dependent stability parameter $a - b$, applied in some of the above studies that consider depth-variable properties, are from wet granite gouge, which has been well studied under hydrothermal conditions but is not a good representation of the oceanic crust. Speculations about reexamination of the rate and state friction data have been proposed by *Liu and Rice* [2007]. In this paper, we apply both wet granite [*Blanpied et al.*, 1998] and recently reported gabbro gouge friction data [*He et al.*, 2007] to a Cascadia-like 2-D subduction fault, to model aseismic transients and compare the resulting surface deformation to GPS observations along the northern Cascadia margin. The major differences between the gabbro and wet granite friction data are (1) velocity weakening to strengthening stability transition occurs at a higher temperature around 510°C for gabbro gouge under supercritical water conditions, compared to ~350°C for wet granite and (2) the absolute values of high-temperature velocity strengthening $a - b$ is approximately 1 order of magnitude smaller for gabbro than for wet granite. When the friction parameters are converted to be depth-variable using a thermal model of the northern Cascadia subduction zone, these differences result in a much deeper friction stability transition, a wider and less stabilizing transition zone for gabbro.

[44] One natural and practical question that arises from the two dramatically different depth distributions of $a - b$ from wet granite and gabbro friction experiments, as shown in Figure 3 (top), is what are their implications for the downdip end of a megathrust earthquake rupture. Using the current model and parameters in Figure 3, for the gabbro friction profile, subduction earthquake rupture propagates beyond the stability transition at ~180 km to downdip ~250 km. The extended propagation in the velocity-strengthening zone is facilitated by the small $a - b > 0$ on the deeper part of the fault. For the wet granite friction profile, earthquake rupture also propagates a bit further downdip from the stability transition (downdip 66 km) to ~85 km, as a result of the highly stabilizing effect of large $a - b > 0$. While no large subduction earthquake has occurred along the Cascadia margin in the past 300 years for a direct measurement, long-term geodetic observations using repeated leveling lines, gravity profiles (time span 4 to 44 years) and tide gauge data (time span 22 to 80 years) are best fit by a completely locked 60 km along-dip segment followed by another 60 km segment with linear increase of slip rate from 0 to V_{pl} [*Dragert et al.*, 1994; *Hyndman and Wang*, 1995]. This would suggest a downdip limit of seismic rupture somewhere between 60 and 120 km. Thus, the gabbro friction data can predict transient slip in reasonable agreement with GPS observations, but also overpredict the downdip extent of seismic rupture indicated by long-term geodetic measurements.

[45] Incorporation of fault gouge dilatancy to the frictional strength evolution appears to be a promising mechanism to reconcile this discrepancy. *Segall and Rice* [1995] showed that fault stabilization by induced suction from dilatancy during accelerated slip becomes most important at extremely high fluid pressure (i.e., low $\bar{\sigma}$), a situation proposed for the occurrence of short-period transients. Including dilatancy in a 2-D subduction fault model with rate and state friction, *Taylor and Rice* [1998] found that quasi-dynamic seismic rupture slows down or even stops near the surface where effective normal stress is lower than that in the seismogenic zone; seismic slip of several meters would occur at the trench without dilatancy. Building on the work by *Taylor and Rice* [1998], *Liu and Rice* [2005b] and especially *Segall and Rubin* [2007], we analyze the conditions for short-period aseismic transients and dimensions of coseismic rupture of a fluid infiltrated subduction fault including dilatancy and pore compaction effects, with a membrane diffusion approximation [*Liu et al.*, 2008]. Not only episodic aseismic transients now exist for a much broader range of W/h^* due to dilatancy stabilization at low $\bar{\sigma}$, the quasi-dynamic seismic rupture speed and spatial extent can also be significantly reduced. Assuming an intermediate fault drainage, i.e., the characteristic diffusion time for fault gouge fluid pressure to reequilibrate with its ambient level is comparable to the characteristic state evolution time, seismic rupture stops updip of the friction stability transition and causes nearly no coseismic slip at the trench, using dilatancy parameters consistent with lab experiments [*Marone et al.*, 1990; *David et al.*, 1994]. This suggests that a subduction fault extending well downdip of the seismogenesis could be frictionally unstable ($a - b < 0$) but undergo no seismic slip due to the existence of high fluid pressure and effective dilatancy stabilization, and provides a possible explanation to the inferred ''gap'' between depths of seismic rupture and slow slip events in northern Cascadia.

5.2. "Ageing" and "Slip" Evolution Laws

[46] As a physical mechanism for episodic slow slip events, fault models using the slip law have generally similar results to those using the ageing law (this paper). Both laws predict fault responses evolving from oscillatory decay, to aseismic simple periodic, complex periodic, and eventually seismic instability as the key parameter W/h^* increases. Spontaneous aseismic oscillations arise at similar W/h^* but are limited within a much smaller range using the slip law than ageing law. For example, for simulation cases with the same subduction fault geometry and friction parameters, *Rubin* [2008] found that transients only appear when W/h^* is between 2 and 4.5 for slip law, and between 2 and 13 for ageing law. This difference may become insignificant with the incorporation of dilatancy, which can effectively delay the onset of seismic instability thus produce aseismic transients at much larger W/h^* [*Liu et al.*, 2008]. Although there are subtle differences in the aseismic ''rupture'' processes modeled with the two evolution laws, aseismic slip in both cases is mostly attributed to the low $\bar{\sigma}$ zone updip from the friction stability transition [*Rubin*, 2008]. In addition, modeling results including normalized maximum moment rate, maximum slip velocity, recurrence interval and cumulative slip during each cycle with the ageing law are in similar ranges to their respective counterparts with the slip law. For both the wet granite and gabbro friction data profiles, parameter space exploration as de-

scribed in section 4 can also be performed using the slip law, to identify appropriate parameter sets that produce aseismic transients of slip and period close to observations. Similarly, we expect model results using the gabbro data can better explain the transient surface deformation in northern Cascadia.

5.3. Two- and Three-Dimensional Simulations

[47] In this study, frictional strength and sliding velocity evolution are calculated as functions of the downdip distance and of time, thus providing a 2-D model. In the evolution process, all properties are assumed to be uniform along the strike direction (plane strain). Cumulative transient slip as a function of depth is extrapolated to slip on a fault plane that spans L_{strike} = 500 km along the strike direction, by assuming an along-strike distribution function. Such a 2-D model setup allows us to explore the parameter space extensively to know how properties such as slip, recurrence interval and maximum velocity change as key parameters W, $\bar{\sigma}$ and L vary in the constrained ranges, for both friction data sets used in this study. Comparisons between GPS observations and numerically predicted surface displacements based on a large group of models are also possible in order to determine the best fitting parameter sets.

[48] Modeling of slow slip events on a 3-D subduction fault governed by rate and state friction has been reported in a previous work [*Liu and Rice*, 2005a] before our recognition of near-lithostatic fluid pressure in SSE source areas; a uniformly high effective normal stress $\bar{\sigma}$ = 100 MPa was used in the entire seismogenic zone and further downdip. Aseismic transients emerge spontaneously around the friction stability transition, and migrate along the strike at speeds much slower than the observed 5–15 km/d in Cascadia. Faster migration was found when $\bar{\sigma}$ reduces to 50 MPa [*Liu and Rice*, 2005b]. Although multiple transients can emerge during the interseismic period, regularly recurring events were not identified in those 3-D simulations with high $\bar{\sigma}$. The near-lithostatic fluid pressure proposition was adopted in a recent 3-D slow slip modeling study by *Shibazaki and Shimamoto* [2007], who used a small cutoff velocity of 10^{-7} to 10^{-6} m/s to control the aseismic slip rate acceleration and deceleration. Under conditions of $\bar{\sigma} \sim$ 1 MPa and $L \sim 0.8$ mm on the deeper plate interface, short-period SSEs with along-strike migration speeds and slip velocities of 4–8 km/d and $2–4 \times 10^{-7}$ m/s, respectively, can be produced. The slow slip along-strike migration speed v_r is found to be proportional to the maximum slip velocity following the relation first obtained by *Ida* [1973] for a mode II elastodynamic rupture

$$\frac{v_r}{V_{\max}} = \gamma \frac{\mu'}{\Delta\tau^{p-r}}, \tag{9}$$

where γ is of order of unity and $\Delta\tau^{p-r}$ is the peak to residual shear stress drop. Equation (9) was also confirmed in the context of slow slip events for along-dip ''rupture'' propagation on a 2-D fault with updip completely locked [*Rubin*, 2008]. The modeled slow slip ''rupture'' in this study, as shown in Figure 8, propagates in both updip and downdip directions, with $v_r \sim$ 3–9 km/d and $V_{\max} \sim 10^{-6}$ to 10^{-7} m/s. As the proportionality between v_r and $V_{\max}$ holds for along-strike propagation, we expect (but cannot verify due to current computational limitations) that in a 3-D model with parameters as presented in this paper lateral migration of slow slip along the trench, like observed in northern Cascadia, would also be produced. The cumulative transient slip distribution from such 3-D models would be more realistic than that extrapolated based on the 2-D models. However, the slow slip would be expected to remain in the same depth range as shown in Figures 10b and 12b, which are determined by the depth-variable model parameters for each friction data set. Thus, the comparisons between observed and modeled surface deformation should be qualitatively similar to what we present here.

6. Conclusion

[49] We apply the ageing version of the rate and state friction law with a single state variable and depth-dependent friction properties to a two-dimensional thrust fault model to simulate episodic slow slip events in shallow subduction zones. Laboratory friction data on wet granite and gabbro gouges are applied to a 2-D fault with a Cascadia-like geometry and thermal profile. Gabbro is an essential part of the oceanic crust and chemically equivalent to basalt, thus a much better proxy than wet granite for the subduction interface studied in this paper. In contrast to the wet granite $\sim$350°C unstable to stable transition, sliding on the gabbro gouge continues to be velocity weakening up to $T \sim 510$°C under supercritical water conditions. The high-temperature velocity-strengthening regime is much less stabilizing than that of wet granite at similar temperatures, due to the nearly 1 order of magnitude smaller $a - b > 0$ up to 600°C. When the friction data are converted to be depth-variable parameters using a thermal model of the northern Cascadia subduction zone, these differences result in a much deeper friction stability transition, with a wider and less stabilizing transition zone for gabbro.

[50] Existence of high fluid pressure in the source areas of slow slip events and nonvolcanic tremors have been suggested by seismological observations, petrological and thermal structures in shallow dipping subduction zones. Near-lithostatic fluid pressure is essential to the occurrence of sustained short-period aseismic oscillations in subduction fault models based on rate and state friction. In this paper, we constrain the depth range of generally overhydrostatic and near-lithostatic fluid pressure zones by incorporating the oceanic crust metamorphic phase diagram and thermal structures of the southwest Japan and northern Cascadia subduction zones. We first identify plausible spatial correspondence between seismically inferred high fluid pressure zone and the depths of major dehydration reactions due to mineral phase changes in the SW Japan subduction zone. Dense instrumentation there such as Hi-net borehole stations has facilitated the precise relocation of nonvolcanic tremors, including low-frequency earthquakes, an indicator of high fluid pressure. An analogy of the spatial correspondence is drawn to the northern Cascadia subduction zone, where dehydration reaction depths are also determined by its petrological and thermal structures, to estimate the distribution of fluid pressure along the interface. Fluid pressure is generally high (overhydrostatic) at depths where major water-releasing phase transitions take place, as well

as the surrounding areas due to fluids permeation. In particular, near-lithostatic fluid pressure is possible around those phase transitions with the most water weight percent reductions, e.g., epidote blueschist to eclogite on the top of the slab and epidote amphibolite to eclogite on the bottom of the slab. The estimated fluid pressure distribution is consistent with inferred high v_p/v_s and Poisson's ratios from at least 20 to 45 km in depth along the northern Cascadia subduction zone from a recent study using converted seismic waveforms [*Audet et al.*, 2009]. The fluid pressure distribution conjecture is further simplified in our model to have an extremely low effective normal stress zone around the friction stability transition, embedded in uniformly high $\bar{\sigma}$ on the rest of the fault (except near the surface).

[51] For a suite of forward models examined, spontaneous aseismic transients emerge within a limited range of W/h^*, which is determined by independently chosen values of W, low $\bar{\sigma}$ and L in consistency with laboratory and observational constraints. W/h^* is $\sim$2 to 7 for wet granite and $\sim$6 to 16 for gabbro. For both friction profiles, the cumulative aseismic slip, recurrence interval and maximum slip velocity increase with W/h^*. Without following a formal inversion procedure and performing true 3-D calculations, we search for parameter sets W, $\bar{\sigma}$ and L that produced aseismic transient of slip 20–30 mm and recurrence interval 1–2 years. L is chosen to be as close to the lab values ($\sim$10s μm) as possible, and extremely small effective normal stress $\bar{\sigma}$ of a few MPa in the transition zone is used. For such simulation cases, we found that aseismic slip nucleates in the velocity-weakening low $\bar{\sigma}$ zone and slip propagates bilaterally at roughly the same speed of 3–9 km/d in both directions before encountering the updip high $\bar{\sigma}$ barrier and downdip stability transition, respectively. Along-strike migration at similar speeds is expected in 3-D calculations with the same parameters. Most of the aseismic slip takes place within the low $\bar{\sigma}$ velocity-weakening zone. Modeled 2-D transient slip and intertransient slip rate are extrapolated to 3-D, assuming an along-strike distribution function, to calculate the surface deformation and deformation rate using *Okada*'s [1992] solution for dislocation in an elastic half-space with constant shear modulus and Poisson's ratio. Transient slip modeled with the wet granite friction data is concentrated in a narrow strip mostly offshore. Except for two coastal stations, only small fractions of the GPS measurements of both transient deformation and intertransient deformation rate at the inland stations can be reproduced. Modeled transient deformation using the gabbro data can fit the GPS measurements fairly well with a fault length of 50 to 55 km updip from the stability transition under low effective normal stress of $\sim$1 MPa and L = 0.16 mm. However, the intertransient deformation rate is generally overpredicted due to the deep interseismic locking at $\sim$100 km downdip. Future experiments on gabbro gouges to measure friction parameters at seismogenic conditions should provide more constraints on the fault locking depth.

[52] Although a more realistic model for such comparisons would incorporate effects such as spatial variations in the geometry and mechanical properties of the subduction slab and the overlying lithosphere, we show that application of reasonably appropriate rate and state friction data has the first order of importance for the forward models to produce results that can be constrained by field observations. For the northern Cascadia subduction margin, friction properties of gabbro gouge seem to do a much better job than the widely used wet granite data. Further laboratory experiments on gabbro and other oceanic crust rocks at elevated temperatures will shed more lights on the mechanism of aseismic deformation transients and possibly nonvolcanic tremors in subduction zones.

[53] **Acknowledgments.** We thank Hiro Noda, who first pointed us to *He et al.*'s [2006] experimental work on gabbro; Changrong He, who provided his then unpublished data and continued discussion on frictional experiments on gabbro gouge; Robert McCaffrey for providing his GPS data analysis; and two anonymous reviewers for their comments that helped to improve the manuscript. We also thank Nora DeDontney for her code to extrapolate a 2-D slip distribution to three dimensions, and we thank Allan M. Rubin and Paul Segall for discussions on effects of dilatancy. This study was initiated at Harvard under support of NSF-EAR award 0510196 and USGS-NEHRP award 07HQGR0057 and continued at Princeton under a Department of Geosciences Hess postdoctoral fellowship to Yajing Liu and USGS-NEHRP award 08HQGR0047 to Allan Rubin that partly supported Y. Liu.

References

Audet, P., M. G. Bostock, N. I. Christensen, and S. M. Peacock (2009), Seismic evidence for overpressured subducted oceanic crust and megathrust fault sealing, *Nature*, *457*, 76–78, doi:10.1038/nature07650.

Bayart, E., A. M. Rubin, and C. Marone (2006), Evolution of fault friction following large velocity jumps, *Eos Trans. AGU*, *87*(52), Fall Meet. Suppl., Abstract S31A-0180.

Beeler, N. M., T. E. Tullis, and J. D. Weeks (1994), The roles of time and displacement in the evolution effect in rock friction, *Geophys. Res. Lett.*, *21*, 1987–1990, doi:10.1029/94GL01599.

Blanpied, M. L., D. A. Lockner, and J. D. Byerlee (1991), Fault stability inferred from granite sliding experiments at hydrothermal conditions, *Geophys. Res. Lett.*, *18*, 609–612, doi:10.1029/91GL00469.

Blanpied, M. L., D. A. Lockner, and J. D. Byerlee (1995), Frictional slip of granite at hydrothermal conditions, *J. Geophys. Res.*, *100*(B7), 13,045–13,064, doi:10.1029/95JB00862.

Blanpied, M. L., C. J. Marone, D. A. Lockner, J. D. Byerlee, and D. P. King (1998), Quantitative measure of the variation in fault rheology due to fluid-rock interactions, *J. Geophys. Res.*, *103*(B5), 9691–9712, doi:10.1029/98JB00162.

Brooks, B. A., J. H. Foster, M. Bevis, L. N. Frazer, C. J. Wolfe, and M. Behn (2006), Periodic slow earthquakes on the flank of Kilauea volcano, Hawai'i, *Earth Planet. Sci. Lett.*, *246*(3–4), 207–216, doi:10.1016/j.epsl.2006.03.035.

Calvert, A. J. (2004), Seismic reflection imaging of two megathrust shear zones in the northern Cascadia subduction zone, *Nature*, *428*(6979), 163–167, doi:10.1038/nature02372.

Chester, F. M., and N. G. Higgs (1992), Multimechanism friction constitutive model for ultrafine quartz gouge at hypocentral conditions, *J. Geophys. Res.*, *97*(B2), 1859–1870, doi:10.1029/91JB02349.

Chlieh, M., J. P. Avouac, K. Sieh, D. H. Natawidjaja, and J. Galetzka (2008), Heterogeneous coupling of the Sumatran megathrust constrained by geodetic and paleogeodetic measurements, *J. Geophys. Res.*, *113*, B05305, doi:10.1029/2007JB004981.

Currie, C. A., R. D. Hyndman, K. Wang, and V. Kostoglodov (2002), Thermal models of the Mexico subduction zone: Implications for the megathrust seismogenic zone, *J. Geophys. Res.*, *107*(B12), 2370, doi:10.1029/2001JB000886.

David, C., T.-F. Wong, W. Zhu, and J. Zhang (1994), Laboratory measurements of compaction-induced permeability change in porous rocks: Implications for the generation and maintenance of pore pressure excess in the crust, *Pure. Appl. Geophys.*, *143*, 425–456, doi:10.1007/BF00874337.

Dieterich, J. H. (1979), Modeling of rock friction 1. Experimental results and constitutive equations, *J. Geophys. Res.*, *84*(B5), 2161–2168, doi:10.1029/JB084iB05p02161.

Dragert, H., R. D. Hyndman, G. C. Rogers, and K. Wang (1994), Current deformation and the width of the seismogenic zone of the northern Cascadia subduction thrust, *J. Geophys. Res.*, *99*(B1), 653–668, doi:10.1029/93JB02516.

Dragert, H., K. Wang, and T. S. James (2001), A silent slip event on the deeper Cascadia subduction interface, *Science*, *292*, 1525–1528, doi:10.1126/science.1060152.

Dragert, H., K. Wang, and G. Rogers (2004), Geodetic and seismic signatures of episodic tremor and slip in the northern Cascadia subduction zone, *Earth Planets Space*, *56*(12), 1143–1150.

Fluck, P., R. D. Hyndman, and K. Wang (1997), Three-dimensional dislocation model for great earthquakes of the Cascadia subduction zone, *J. Geophys. Res.*, *102*(B9), 20,539–20,550, doi:10.1029/97JB01642.

Gomberg, J., J. L. Rubinstein, Z. Peng, K. C. Creager, J. Vidale, and P. Bodin (2008), Widespread triggering of nonvolcanic tremor in California, *Science*, *319*, 173 , doi:10.1126/science.1149164.

Hacker, B. R., G. A. Abers, and S. M. Peacock (2003), Subduction factory 1. Theoretical mineralogy, densities, seismic wave speeds, and H_2O contents, *J. Geophys. Res.*, *108*(B1), 2029, doi:10.1029/2001JB001127.

He, C., W. Yao, Z. Wang, and Y. Zhou (2006), Strength and stability of frictional sliding of gabbro gouge at elevated temperatures, *Tectonophysics*, *427*, 217–229, doi:10.1016/j.tecto.2006.05.023.

He, C., Z. Wang, and W. Yao (2007), Frictional sliding of gabbro gouge under hydrothermal conditions, *Tectonophysics*, *445*, 353–362, doi:10.1016/j.tecto.2007.09.008.

Hirose, H., K. Hirahara, F. Kimata, N. Fujii, and S. Miyazaki (1999), A slow thrust slip event following the two 1996 Hyuganada earthquakes beneath the Bungo Channel, southwest Japan, *Geophys. Res. Lett.*, *26*, 3237–3240, doi:10.1029/1999GL010999.

Hyndman, R. D., and K. Wang (1995), The rupture zone of Cascadia great earthquakes from current deformation and the thermal regime, *J. Geophys. Res.*, *100*(B11), 22,133–22,154, doi:10.1029/95JB01970.

Ida, Y. (1973), The maximum acceleration of seismic ground motion, *Bull. Seismol. Soc. Am.*, *63*, 959–968.

Ide, S., D. R. Shelly, and G. C. Beroza (2007), Mechanism of deep low frequency earthquakes: Further evidence that deep non-volcanic tremor is generated by shear slip on the plate interface, *Geophys. Res. Lett.*, *34*, L03308, doi:10.1029/2006GL028890.

Kao, H., S. Shan, H. Dragert, G. Rogers, J. F. Cassidy, and K. Ramachandran (2005), A wide depth distribution of seismic tremors along the northern Cascadia margin, *Nature*, *436*, 841–844, doi:10.1038/nature03903.

Kao, H., S. Shan, H. Dragert, G. Rogers, J. F. Cassidy, K. Wang, T. S. James, and K. Ramachandran (2006), Spatial-temporal patterns of seismic tremors in northern Cascadia, *J. Geophys. Res.*, *111*, B03309, doi:10.1029/2005JB003727.

Kato, N. (2003), A possible model for large preseismic slip on a deeper extension of a seismic rupture plane, *Earth Planet. Sci. Lett.*, *216*(1–2), 17–25, doi:10.1016/S0012-821X(03)00483-7.

Kato, N., and T. Hirasawa (1997), A numerical study on seismic coupling along subduction zones using a laboratory-derived friction law, *Phys. Earth Planet. Inter.*, *102*(1–2), 51–68, doi:10.1016/S0031-9201(96)03264-5.

Kodaira, S., T. Iidaka, A. Kato, J. O. Park, T. Iwasaki, and Y. Kaneda (2004), High pore fluid pressure may cause silent slip in the Nankai trough, *Science*, *304*, 1295–1298, doi:10.1126/science.1096535.

Lachenbruch, A. H., and J. H. Sass (1973), Thermo-mechanical aspects of the San Andreas Fault system, in *Proceedings of the Conference on the Tectonic Problems of the San Andreas Fault System*, edited by B. L. Kovach and A. Nur, *Stanford University Publ. Geol. Sci.*, *13*, 192–205.

Lapusta, N., and J. R. Rice (2003), Nucleation and early seismic propagation of small and large events in a crustal earthquake model, *J. Geophys. Res.*, *108*(B4), 2205, doi:10.1029/2001JB000793.

Lapusta, N., J. R. Rice, Y. Ben-Zion, and G. Zheng (2000), Elastodynamic analysis for slow tectonic loading with spontaneous rupture episodes on faults with rate- and state-dependent friction, *J. Geophys. Res.*, *105*(B10), 23,765–23,789, doi:10.1029/2000JB900250.

La Rocca, M., K. C. Creager, D. Galluzzo, S. Malone, J. E. Vidale, J. R. Sweet, and A. G. Wech (2009), Cascadia tremor located near plate interface constrained by S minus P wave times, *Science*, *323*, 620–623, doi:10.1126/science.1167112.

Linde, A. T., M. T. Gladwin, M. J. S. Johnston, R. L. Gwyther, and R. G. Bilham (1996), A slow earthquake sequence on the San Andreas fault, *Nature*, *383*(6595), 65–68, doi:10.1038/383065a0.

Liu, Y., and J. R. Rice (2005a), Aseismic slip transients emerge spontaneously in three-dimensional rate and state modeling of subduction earthquake sequences, *J. Geophys. Res.*, *110*, B08307, doi:10.1029/2004JB003424.

Liu, Y., and J. R. Rice (2005b), Pore pressure evolution in shallow subduction earthquake sequences and effects on aseismic slip transients—Numerical modeling with rate and state friction, *Eos Trans. AGU*, *86*(52), Fall Meet. Suppl., Abstract T11E-05.

Liu, Y., and J. R. Rice (2007), Spontaneous and triggered aseismic deformation transients in a subduction fault model, *J. Geophys. Res.*, *112*, B09404, doi:10.1029/2007JB004930.

Liu, Y., A. M. Rubin, J. R. Rice, and P. Segall (2008), Role of fault dilatancy in subduction zone aseismic deformation transients and thrust earthquakes, *Eos Trans. AGU*, *89*(53), Fall Meet. Suppl., Abstract S34B-04.

Lockner, D. A., and J. D. Byerlee (1986), Laboratory measurements of velocity-dependent frictional strength, *U.S. Geol. Surv. Open File Rep., 86-417*.

Lowry, A. R., K. M. Larson, V. Kostoglodov, and R. Bilham (2001), Transient fault slip in Guerrero, southern Mexico, *Geophys. Res. Lett.*, *28*, 3753–3756, doi:10.1029/2001GL013238.

Marone, C., C. B. Raleigh, and C. H. Scholz (1990), Frictional behavior and constitutive modeling of simulated fault gouge, *J. Geophys. Res.*, *95*(B5), 7007–7025, doi:10.1029/JB095iB05p07007.

Mazzotti, S., H. Dragert, J. Henton, M. Schmidt, R. Hyndman, T. James, Y. Lu, and M. Craymer (2003), Current tectonics of northern Cascadia from a decade of GPS measurements, *J. Geophys. Res.*, *108*(B12), 2554, doi:10.1029/2003JB002653.

McCaffrey, R. (2009), Time-dependent inversion of three-component continuous GPS for steady and transient sources in northern Cascadia, *Geophys. Res. Lett.*, *36*, L07304, doi:10.1029/2008GL036784.

Miyazawa, M., and J. Mori (2006), Evidence suggesting fluid flow beneath Japan due to periodic seismic triggering from the 2004 Sumatra-Andaman earthquake, *Geophys. Res. Lett.*, *33*, L05303, doi:10.1029/2005GL025087.

Murray, J. R., and P. Segall (2005), Spatiotemporal evolution of a transient slip event on the San Andreas fault near Parkfield, California, *J. Geophys. Res.*, *110*, B09407, doi:10.1029/2005JB003651.

Obara, K. (2002), Nonvolcanic deep tremor associated with subduction in southwest Japan, *Science*, *296*, 1679–1681, doi:10.1126/science.1070378.

Okada, Y. (1992), Internal deformation due to shear and tensile faults in a half-space, *Bull. Seismol. Soc. Am.*, *82*(2), 1018–1040.

Peacock, S. M., K. Wang, and A. M. McMahon (2002), Thermal structure and metamorphism of subducting oceanic crust: Insight into Cascadia intraslab earthquakes, in *The Cascadia Subduction Zone and Related Subduction Systems: Seismic Structure, Intraslab Earthquakes and Processes, and Earthquake Harzards*, edited by S. Kirby, K. Wang, and S. Dunlop, *U.S. Geol. Surv. Open File Rep.*, *02-328*, 123–126.

Peng, Z., and K. Chao (2008), Nonvolcanic tremor beneath the Central Range in Taiwan triggered by the 2001 M_w 7.8 Kunlun earthquake, *Geophys. J. Int.*, *175*(2), 825–829, doi:10.1111/j.1365-246X.2008.03886.x.

Peng, Z., J. E. Vidale, K. C. Creager, J. L. Rubinstein, J. Gomberg, and P. Bodin (2008), Strong tremor near Parkfield, CA, excited by the 2002 Denali Fault earthquake, *Geophys. Res. Lett.*, *35*, L23305, doi:10.1029/2008GL036080.

Rice, J. R. (1992), Fault stress states, pore pressure distributions, and the weakness of the San Andreas Fault, in *Fault Mechanics and Transport Properties of Rocks*, edited by B. Evans and T.-F. Wong, pp. 475–503, Elsevier, New York.

Rice, J. R. (1993), Spatiotemporal complexity of slip on a fault, *J. Geophys. Res.*, *98*(B6), 9885–9907, doi:10.1029/93JB00191.

Rice, J. R., and Y. Ben-Zion (1996), Slip complexity in earthquake fault models, *Proc. Natl. Acad. Sci. U. S. A.*, *93*(9), 3811–3818, doi:10.1073/pnas.93.9.3811.

Rice, J. R., N. Lapusta, and K. Ranjith (2001), Rate and state dependent friction and the stability of sliding between elastically deformable solids, *J. Mech. Phys. Solids*, *49*, 1865–1898, doi:10.1016/S0022-5096(01)00042-4.

Rogers, G., and H. Dragert (2003), Episodic tremor and slip on the Cascadia subduction zone: The chatter of silent slip, *Science*, *300*, 1942–1943, doi:10.1126/science.1084783.

Rubin, A. M. (2008), Episodic slow slip events and rate-and-state friction, *J. Geophys. Res.*, *113*, B11414, doi:10.1029/2008JB005642.

Rubinstein, J. L., J. Vidale, J. Gomberg, P. Bodin, K. C. Creager, and S. Malone (2007), Non-volcanic tremor driven by large transient shear stresses, *Nature*, *448*, 579–582, doi:10.1038/nature06017.

Ruina, A. L. (1983), Slip instability and state variable friction laws, *J. Geophys. Res.*, *88*(B12), 10,359–10,370, doi:10.1029/JB088iB12p10359.

Scholz, C. H. (2002), *The Mechanics of Earthquakes and Faulting*, 2nd ed., Cambridge Univ. Press, Cambridge, U. K.

Schwartz, S. Y., and J. M. Rokosky (2007), Slow slip events and seismic tremor at circum-Pacific subduction zones, *Rev. Geophys.*, *45*, RG3004, doi:10.1029/2006RG000208.

Segall, P., and J. R. Rice (1995), Dilatancy, compaction, and slip instability of a fluid-infiltrated fault, *J. Geophys. Res.*, *100*(B11), 22,155–22,171, doi:10.1029/95JB02403.

Segall, P., and A. Rubin (2007), Dilatancy stabilization of frictional sliding as a mechanism for slow slip events, *Eos Trans. AGU*, *88*(52), Fall Meet. Suppl., Abstract T13F-08.

Segall, P., E. K. Desmarais, D. R. Shelly, A. Miklius, and P. Cervelli (2006), Earthquakes triggered by silent slip events on Kilauea volcano, Hawaii, *Nature*, *442*, 71–74, doi:10.1038/nature04938.

Shelly, D. R., G. C. Beroza, S. Ide, and S. Nakamula (2006), Low-frequency earthquakes in Shikoku, Japan, and their relationship to episodic tremor and slip, *Nature*, *442*, 188–191, doi:10.1038/nature04931.

Shelly, D. R., G. C. Beroza, and S. Ide (2007), Non-volcanic tremor and low-frequency earthquake swarms, *Nature*, *446*, 305–307, doi:10.1038/nature05666.

Shibazaki, B., and Y. Iio (2003), On the physical mechanism of silent slip events along the deeper part of the seismogenic zone, *Geophys. Res. Lett.*, *30*(9), 1489, doi:10.1029/2003GL017047.

Shibazaki, B., and T. Shimamoto (2007), Modelling of short-interval silent slip events in deeper subduction interfaces considering the frictional properties at the unstable-stable transition regime, *Geophys. J. Int.*, *171*(1), 191–205, doi:10.1111/j.1365-246X.2007.03434.x.

Shimamoto, T. (1986), Transition between frictional slip and ductile flow for halite shear zones at room-temperature, *Science*, *231*, 711–714, doi:10.1126/science.231.4739.711.

Stesky, R. M. (1975), The mechanical behavior of faulted rock at high temperataure and pressure, Ph.D. thesis, Mass. Inst. of Technol., Cambridge.

Taylor, M. A. J., and J. R. Rice (1998), Dilatant stabilization of subduction earthquake rutpure into shallow thrust interface, *Eos Trans. AGU*, *79*(45), Fall Meet. Suppl., F631.

Tse, S. T., and J. R. Rice (1986), Crustal earthquake instability in relation to the depth variation of frictional slip properties, *J. Geophys. Res.*, *91*(B9), 9452–9472, doi:10.1029/JB091iB09p09452.

Wada, I., K. Wang, J. He, and R. D. Hyndman (2008), Weakening of the subduction interface and its effects on surface heat flow, slab dehydration, and mantle wedge serpentinization, *J. Geophys. Res.*, *113*, B04402, doi:10.1029/2007JB005190.

Weeks, J. D., and T. E. Tullis (1985), Frictional sliding of dolomite: A variation in constitutive behavior, *J. Geophys. Res.*, *90*(B9), 7821–7826, doi:10.1029/JB090iB09p07821.

Y. Liu, Department of Geosciences, Princeton University, 308A Guyot Hall, Princeton, NJ 08544, USA. (yjliu@princeton.edu)

J. R. Rice, Department of Earth and Planetary Sciences, Harvard University, 224 Pierce Hall, 29 Oxford Street, Cambridge, MA 02138, USA. (rice@seas.harvard.edu)